Flettner rotor Propulsion measurement and validation

Mechanical engineering
Master's thesis
Department of Mechanical and Materials Engineering

Author(s):
Mikko Aleksander Gävert

16.6.2026
Turku

Master's thesis

Subject: Mechanical engineering
Author(s): Mikko Aleksander Gävert
Title: Flettner rotor Propulsion measurement and authentication
Supervisor(s): Prof. Wallace Moreira Bessa
Number of pages: 56 pages
Date: 1.7.2026

Flettner Rotors are a wind-assisted propulsion method experiencing renewed commercial interest, which is driven by increasingly tightening maritime emission regulations. Flettner rotors have seen a surge of usage in recent years. This thesis evaluates the propulsion measurement and estimation methods applicable to Flettner Rotors, and validates the reliability of the pressure-sensor-based system deployed on Norsepower RotorSails through experimental testing and CFD comparison. The study combines a qualitative literature review of Flettner rotor History, magnus effect fluid dynamics, and measurement principles, with a quantitative validation study using real world wind test data collected at the Norsepower test site in Naantali, Finland in April 2026. Three tests were designed: signal quality assessment using a pulse generator, a phase-change analysis of the pressure matrix, and a cross-method comparison of pressure sensor data against CFD simulations. Of these Three tests Two were successfully completed, leaving the phase change analysis of pressure matrixes for further study. A 50Hz interference signal was found, but its amplitude was found to be small enough to confirm the signal to be of acceptable quality. By comparing the CFD simulated data at each RS height segment and by applying stricter data acceptance filters the deviation between measured and simulated force magnitudes was brought down from approx. 12% to approx. 5%. The remaining discrepancy is attributed primarily to windshear function incorrectness, more specifically the ground shear boundary layer exponent inaccuracy. The result confirm that the Norsepower RS propulsion measurement system produces reliable force data. The Identified sources of residual error provide a clear direction to improving simulations in the future.

Key words: Flettner Rotor, rotor sail, wind-assisted ship propulsion, pressure measurement, CFD validation, Signal quality, wind shear, Magnus Effect.

Q1: What type of propulsion measurements are applicable to Flettner Rotors? (4. Propulsion measurement methods)

Q2: How to detect temporal lag in measurements? (7.1Test 1, pressure sensors emulation and 7.2 Test 2: Pressure matrix phase change)

Q3: How to authenticate the results of measurements? (7.3. Test 3, comparing all data across all measuring methods.)

Table of contents

1 Introduction

A Flettner rotor is a mechanical device which obtains a spinning cylinder that creates a pressure differential across its surface, creating a force vector. In shipping context, a Flettner Rotor is referred as Rotor Sail, given its sail-like properties as wind propulsion. The Flettner rotor was named after its inventor Anton Flettner, who patented it in 1922 [1]. The Flettner Rotor uses the principles of the Magnus effect[2], named after its discoverer Heinrich Gustav Magnus (1802 - 1870), who discovered that a spinning object creates pressure differentials across its surface[2]. With the Magnus effect the sail can produce a lift vector, whose direction can be determined by spin-direction. The lift vector is roughly perpendicular to the oncoming air. The Flettner rotor has found application in the marine environment over the past decade. The first proof of concept was demonstrated in the year 1925, when an old Schooner was retrofitted with two of these rotors. Canvas-based sails were used for propulsion for centuries before they were displaced out by first the coal-fired steam engines and then subsequently superseded by more efficient diesels engines, which still hold their position as the main propulsive power for ships to this day. This transition was driven by the wide availability and low cost of fossil fuels, which enabled the operation of faster vessels with reduced crew requirements. However, the era of fossil fuels is gradually transitioning to other renewable and more green energy sources. Recent years in maritime have been characterized by high fuel prices and increasingly strict emissions regulations[3]. Most notably due to the Energy Efficiency Design Index (EEDI) by the International Maritime Organization's (IMO) Marine Environment Protection Committee (MEPC) with its latest update in 2022 (IMO, 2022). By 2030 the CO2 emissions per transport work is to be reduced by 40% compared to the level from 2008 according to MEPC's vision [4]. While these regulations take effect, shipping companies are retrofitting their fleets with greener solutions. Although Flettner rotors are not feasible as the only source of propulsive power, their merits as a fuel-saving auxiliary to conventional propulsion systems have been recognised [5]. Compared to traditional sails, Flettner rotors have the advantage of being smaller and structurally fixed as they do not need active trimming and hoisting. Unlike traditional sails, Flettner rotors require no attention from the crew, but do need electrical power for rotating the cylinder. Despite over a century of validated aerodynamic principles and a clear regulatory incentive, wind-assisted propulsion systems are underutilized. While commercial interest has grown in resent years, broader adaptation is hindered not only by economic considerations, but also by uncertainty surrounding the reliability of the propulsion measurement systems. This thesis evaluates the propulsion measurement and estimation methods applicable to Flettner Rotors, and validates the reliability of the pressure-sensor-based system deployed on Norsepower RotorSails through experimental testing and CFD comparison. The research addresses three main questions. Q1: What type of propulsion measurements are applicable to Flettner Rotors? Q2: How to detect temporal lag in measurements? Q3: How to authenticate the results of measurements? Chapters 2-4 establish the theoretical basis on different propulsion methods using a methodology of further experiments that are based on the earlier research, these experiments are run on Norsepower Naantali Test-site (NaTe or NATE). Q2 is addressed in test 1 and it is further explored in theoretical means in the proposed test: "*7.2 Test 2: Pressure matrix phase change*", which was not preformed. Q3 is addressed with numerical analysis of data in test 3.

2 Background

To understand the technology behind the Flettner Rotor it is important to understand the discovery, history, and how the technology has matured. This section provides the reader a basic understanding of the history and how the Flettner Rotor became what it is today. It also explains why and when this technology has been used and why the technology has not achieved widespread adaptation despite its concept having been validated experimentally and mathematically throughout history.

2.1 Magnus effect

The magnus effect was named after its discoverer, Gustaf Magnus. He was a professor at the University of Berlin from 1834 to 1869. His experiment that revealed the aerodynamic effect was conducted in 1852, in which Magnus had a spinning brass cylinder mounted on freely spinning stand. In the arrangement of his setup, he could spin up the cylinder around its own axis and direct air flow at it, revealing the created lift force that rotated the stand. Magnus observed that the cylinder pulled the arm towards the flow of air, contrary to the logic of point of pressure trying to move away from the flow, concluding that a lateral force was applied to the test stand. Although Magnus did not quantify the forces involved, his qualitative observations demonstrated the existence of a lift force generated by rotation in a fluid flow. This phenomenon has since become known as the Magnus effect[6]. In 1877 Lord John Rayleigh wrote an article about a tennis ball and its flight path. In his article he states that at that time it was not possible to give complete mathematical formulation of the physics behind the magnus effect. Even though the Navier-Stokes formula was already known, there was no established knowledge of boundary layers and their properties, and no numerical methods to solve the magnus effect. In 1912 A.Laffay wrote an article about rotating cylinders and concluded in his experiments that their lift output could be much greater than air foils of the same projected area. Later in 1918 Herman Föttinger wrote an article in which he discussed experiments relating to the lateral forces acting upon rotating cylinders placed in an airflow. He concluded that a rotating cylinder behaved aerodynamically similarly to an inclined plate in an airflow.[7] In 1919 an attempt was made to create a propeller with rotating cylinders as blades. It was a successful proof of concept, but it did not perform as well as a traditional propeller. With the problem of spinning the cylinders while mounted on a rotating base, the system was much too difficult compared to an ordinary propeller. The most notable attempt to use the high lift forces obtainable on a spinning cylinder in an airstream was made by Anton Flettner in Germany in the 1920s. Flettner consulted with Ludwig Prandtl and the Göttingen research group on the idea of replacing the sail of a vessel with rotors. In a cross wind, the Magnus effect would produce a thrust many times that for an equivalent sail area. The idea showed promise, and thus was born the Flettner rotor, named after Anton Flettner.

2.2 Flettner rotor

The use of the Magnus effect did not take off in the aviation sector, as the rotating cylinder proved too complicated in this application. In the 1920s, Anton Flettner gathered a research group to create now well-known Flettner rotor. He had the idea of using a rotating cylinder with endplates to enhance sailing properties of sailing ships. By using endplates, the Flettner rotor could improve its aerodynamic properties near the ends of the cylinder, by lessening created vortices of the lifting surface. The principle of the endplate is much similar that of a winglet that is used in today's aviation to reduce wing tip vortices, and thus increase the Lift to Drag ratio [8]. Anton Flettner tried to create the perfect sailing vessel with his patented rotors. The first prototype ship was the Schooner Buckau. She served as an effective proof of concept for the Flettner rotor system though with limited operational success. The whole rigging of the ship was retrofitted with two Flettner rotors of 15m in height and 3m in diameter. These rotors had a considerably smaller projected area compared to the old rigging and its canvas-area, see Figure [9] top left corner. The first sea trials showed that with a 20hp electric system that spun the Flettner rotors could output 1000hp equivalent of thrust. As Figure shows, the rotor sails had relatively same propulsion amplitude as the old rigging, but their active lift area, the cross area of the rotor, was a lot smaller in comparison. The two graphs in Figure 1 represent force resultants created at different wind directions. The figure is read by turning the heading of the ship "*Cap part rapport ai vent apparent*", which in turn changes the apparent wind "*Vent apparent*". The distance of the graph at that heading to the origo of the graph will tell the force resultant. In some cases, the old rigging was better, such as with wind apparent close to 90° and at tailwinds. The reason for old canvas having the advantage at 90° is because at that angle, all masts have the most sail area exposed to the wind. And at tail wind the most efficient way is to open the canvas as a parachute, creating as much drag as possible. At exact 180 degree angle the Flettner Rotors do not benefit from spinning, as their lift vector is perpendicular to the velocity vector. The only thing the rotors could produce at those angles is drag, that can be produced at non-spinning position as well. But as an all-around system the Flettner rotors proved better. Some reports stated that the cruising speed of Buckau was raised from 6.2kt to 8kt.[10]

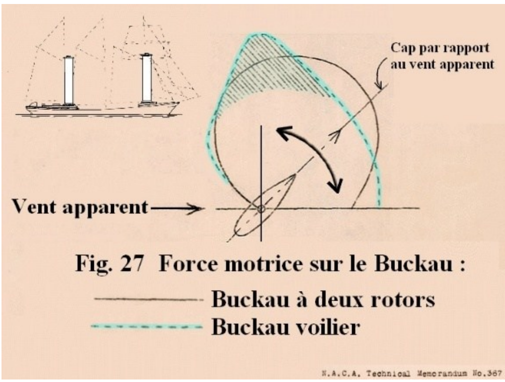

Figure 1: Propulsion chart of Buchau and comparison of sail area between RS and Canvas

"The schooner Buckau recently put out to sea, a ship without sails or steam. Like a ghost ship it moved mysteriously through the water with no apparent means of propulsion. ... The astounded spectators on shore knew that the boat was an old 700-ton steel vessel and that previously 500 square yards of canvas had been needed to propel her. ... Two strange cylinders, resembling giant smokestacks, rose from her deck. But no smoke was pouring from them, and no engine noise was heard. There was no churning of screws. Yet the ship plowed its way through the rough waters of the Baltic, at nearly twice its former speed." [11]
The whole Flettner rotor system was 1/5th of the weight of the old rigging, fuel, electric and rotor systems combined. Other reports stated that the system required less crew to operate, making the Buckau easier to handle with the new propulsion system. Other benefits included the handling in rough seas. Reports state that the ship leaned into the wind, contrary to normal rigging that leaned with it. This statement could be considered true when examining the resultant force created by the Flettner rotor. This will be reviewed later in more detail, but the Flettner Rotor creates a resultant force vector around 90 degrees compared to the wind. Should the wind come from +90 degrees the force vector would lean the ship to its wind side. The same reports found on this early prototype state that this effect made the ship's hull more stable. With this ability the Flettner rotor creates more reliable ships, which can be more stable in heavy weather. One of the most successful ships to demonstrate this effect is the Sea Cargo Connector. She sails on the North Sea and Rotor Sails have stabilised the ships passage. Reports state that the ship is more likely to arrive on time, thanks to the Rotor Sail, and the maximum wind and wave limits have been lifted after the installation.[12]

In 1926 the schooner Buckau, now renamed Baden Baden, sailed to New York via South America. The 6,200 nautical mile voyage across the Atlantic used only 12 tons of fuel oil, compared with 45 tons for a motor ship of the same size without rotors.[11] This was the first long voyage of a ship installed with the Flettner rotor, and it proved the fuel efficiency of the system. Anton Flettner had another ship retrofitted with Flettner rotors to test out the properties of his invention. In 1926 the German navy commissioned the second rotor ship Barbara, 2000 tonnes. She served as a conventional freighter in the Mediterranean from 1926 to 1929. By 1928 Anton Flettner had secured orders for six more of Barbara class ships, but these orders were revoked as of the great financial crash of 1929 that limited any new shipbuilding, and with the technological advances in marine engine technology the financial case of building vessels with Flettner rotors were phased out.

2.3 Re-emergence in maritime use

The interest around Flettner rotors has re-emerged as of late. During the 2010s, both European Union (EU) and International Maritime organization (IMO) have put-up ever-increasing greenhouse gas emissions regulations. The EU has plans to cut ship greenhouse emissions by 80% of the 2020 levels by 2050[13]. These objectives can be achieved in numerous ways. One of which is the onshore power supply systems. This technology links the ships own power grid to the shore power grid, making it possible to shut off all generators on board, thereby eliminating all emissions while being loaded/unloaded. Ships sometimes spend multiple days on shore when loading and unloading. Not only does this reduce the emissions it also gives the crew the ability to service the generators. To comply with the increasing regulations shipowners must adopt other technologies as well. The most promising is new maritime engines, which achieve better fuel efficiency, use better fuels, and use better scrubbers. All of these positive aspects combine a greener system altogether. But as the Flettner rotor technology uses electricity created by the ship and multiplies its propulsion power it builds up the vessel's overall efficiency. Installations such as the RoRo vessel Sea Cargo Connector have shown that Flettner Rotors can produce up to 5.5MW equivalent of motor shaft propulsion using just 220kW of electric power [14]. Some tests have shown that a bulk carrier can propel itself with its main engine completely off, using just the propulsion of RotorSails. Flettner rotor manufacturers such as Norsepower and Anemoi report projected 5-25% fuel consumption reduction across the lifespan of operations from a ship.

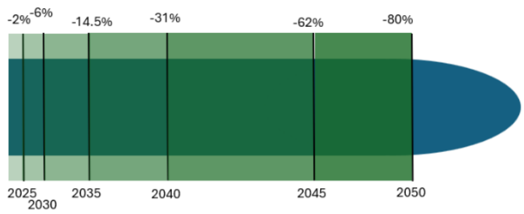

Figure 2: EU plan of cutting emissions comparing to 2010

Renewed interest in Flettner rotors emerged following the introduction of the IMO's Energy Efficiency Existing Ship Index (EEXI) [15]. This regulation incentivized shipowners to retrofit their ships with existing technology that aims to improve the vessels overall efficiency. Such technologies are the advanced flaperon rudders and new propellers. Wind assisted propulsion is viewed as a supplementary strategy. The first commercial vessel to use Flettner Rotors was E-ship 1. This Vessel was built and maintained by Enercon and used to build windfarms near the coast of south America. She was launched in 2008 and designed to carry windfarm turbine components. The ship reported that the Flettner rotors contributed 38% of the total propulsive power when sailing at 16.7kt. A validation case of the coast of Brazil showed that over 80% of the ship's propulsion was made with the rotors with wind speed of 13.5m/s.

3 Fluid dynamics and properties of Flettner Rotors

Understanding the freestream flow is essential to explain how a rotor sail functions and, consequently, how to measure its propulsive performance. The Flettner rotor generates aerodynamic lift through the Magnus effect. When a cylinder rotates at high angular velocity in an external airflow, the viscous interaction between the cylinder surface and the surrounding fluid modifies the boundary layer and alters the velocity distribution around the cylinder. On one side of the cylinder, the surface motion aligns with the freestream flow, increasing the local air velocity. On the opposite side, the surface motion opposes the freestream, reducing the local velocity (Figure 3). This asymmetry in velocity produces a pressure difference around the cylinder. According to Bernoulli's equation for incompressible flow:

$$P + \rho g h + \frac{1}{2}\rho v^2 = \text{constant}$$

where P is pressure, ρ is fluid density, g is the gravitational acceleration, h is elevation, and v is flow velocity. In typical aerodynamic applications, elevation changes are negligible. Therefore, an increase in flow speed corresponds to a decrease in static pressure. As a result, the side of the rotor, on which the flow velocity is higher, experiences lower pressure, while the opposite side experiences higher pressure. This pressure imbalance produces a force perpendicular to the incoming flow, which constitutes the lift generated by the Magnus effect. The resultant force of this phenomenon combines lift and drag, which result in under 90-degree difference in the force vector direction and free stream velocity direction. The mechanism is analogous to lift generation on a conventional airfoil, where circulation and velocity differences between the upper and lower surfaces create a pressure differential. In the case of the Flettner rotor, however, the circulation is generated primarily by active rotation rather than by the airfoil geometry alone. As is typical for rotating cylinders, the Magnus force can be resolved into a lift component perpendicular to the incoming flow and a drag component parallel to the flow. The friction between the rotor surface and the surrounding fluid also generates torque, which must be overcome by a mechanical drive to maintain rotation [6].

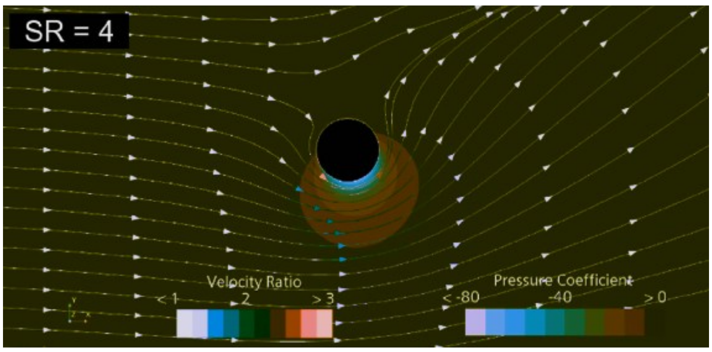

Figure 3: Fluid flow field around RS when SpinRatio = 4

As with an airfoil in freestream flow, the total aerodynamic force acting on a Flettner rotor can be decomposed into two orthogonal components: lift (L), the component perpendicular to the freestream velocity and drag (D), the component parallel to the freestream velocity.

Both forces are commonly expressed using nondimensional coefficients:

$$L = \frac{1}{2}\rho V^2 A C_L$$

$$D = \frac{1}{2}\rho V^2 A C_D$$

where: ρ= air density, V= freestream velocity, A= reference area (rotor height × diameter), C_L= lift coefficient, C_D= drag coefficient

Unlike a fixed airfoil, a rotating cylinder can achieve very high lift coefficients because rotation actively controls the circulation strength around the body. [16]

A key non-dimensional parameter governing the aerodynamic performance of a Flettner rotor is the SpinRatio (SR). The spin ratio represents the relationship between the tangential surface velocity of the rotating cylinder and the freestream wind velocity. It is defined as

$$SR = \frac{\omega R}{V}$$

where

ω= angular velocity of the rotor (rad/s),

R= rotor radius (m),

V= freestream wind speed (m/s).

In aerodynamic literature, this parameter is sometimes referred to as the velocity ratio, which is mathematically equivalent and describes the same physical relationship between surface speed and incoming flow velocity. The spin ratio is a primary scaling parameter for the Magnus effect, which is responsible for the generation of lift on a rotating cylinder. As the Magnus effect is based on the creation of a boundary layer on the surface of Flettner Rotors, the relative speed of the airflow to said surface speed greatly dictates the magnitude of Magnus effect. Both the lift coefficient (C_L) and drag coefficient (C_D) are strongly dependent on SR, making it one of the most important variables in Flettner rotor performance prediction. According to *"A Parametric Study for a Flettner Rotor in Standalone Condition Using CFD"* [8], computational fluid dynamics (CFD) simulations demonstrate that increasing the spin ratio generally leads to an increase in both lift and drag coefficients within a moderate operating range. However, beyond a certain threshold (approximately SR ≈ 4 for the rotor geometry studied), further increases in SR do not yield proportional gains, instead the Lift to Drag

ratio (L/D) starts to plateau. As L/D ratio does not increase, increasing spin in the rotor would only increase the energy consumption of the system bringing overall efficiency down. This suggests the existence of an optimal spin ratio range for maximizing aerodynamic force production.
The same study also highlights important changes in the flow field as SR increases. At low spin ratios, the wake is characterized by strong vortex shedding and unsteady flow behaviours, which can lead to fluctuating aerodynamic forces. As SR increases, the flow transitions toward a more quasi-steady regime, reducing wake instability and producing more stable thrust forces. Despite these aerodynamic benefits, studies note that energy efficiency decreases at higher SR values [16], [17], [18]. This is because the mechanical power required to overcome viscous and aerodynamic torque grows more rapidly than the useful aerodynamic lift generated.

Similar conclusions are presented in *"Flettner Rotor Concept for Marine Applications: A Systematic Study"* [7]. In this work, the aerodynamic coefficients were systematically evaluated as functions of spin ratio across a range of rotor geometries. The results confirm that lift and drag coefficients increase with SR over the practical design range. The study further developed surrogate mathematical models that relate $C_L$and $C_D$directly to SR, enabling performance prediction during preliminary design stages. However, the authors emphasize that rotor efficiency and force generation are also influenced by geometric parameters such as aspect ratio and end-plate configuration, meaning that SR must be considered as part of a broader aerodynamic design space.

Studies identify the spin ratio as a dominant parameter in Flettner rotor aerodynamics. Increasing SR enhances the Magnus effect and raises both lift and drag coefficients up to an optimal range, beyond which performance gains diminish and energy efficiency declines. Additionally, higher spin ratios contribute to more stable aerodynamic behaviour by reducing unsteady wake effects. These findings establish SR as a central design variable in the aerodynamic and energetic optimization of Flettner rotor systems.

The development of the boundary layer on a Flettner rotor is strongly influenced by the Reynolds number (Re), which governs the relative importance of inertial and viscous forces in the flow. At lower Re, the boundary layer is thicker and more susceptible to separation, reducing the effective lift and increasing drag. As Re increases toward critical and supercritical regimes, the boundary layer becomes thinner and more stable, delaying flow separation and enhancing aerodynamic performance[19]. For propulsion measurements using surface pressure sensors, these boundary layer effects are critical: variations in Re alter the local pressure distribution, meaning that lift and drag coefficients derived from small-scale experiments or low-Re flow conditions may not directly translate to full-scale operating conditions. The wake downstream of a Flettner rotor is shaped by both spin ratio and boundary layer characteristics, and it plays a major role in the temporal and spatial variability of measured forces. At lower Reynolds numbers or under conditions of strong vortex shedding, the wake is highly unsteady, producing significant fluctuations in surface pressure signals. As the flow becomes more stable and the boundary layer adheres better to the rotor surface, wake turbulence diminishes, resulting in a more coherent and quasi-steady flow. From the perspective of pressure sensor–based propulsion measurement, wake turbulence directly affects data integrity, but its effect is diminished when inspecting averages. As the propulsion estimate is created by taking multiple samples on the surface and creating a mean pressure matrix over time, the effect of turbulence is reduced. Furthermore, nearby structures, such as ship cranes, containers etc. will affect both wake and freestream properties. This effect will be noted in the upcoming tests.

4 Propulsion measurement methods

This section presents the propulsion measurement methods applicable to Flettner rotor systems. At the time of writing there are a few methods known publicly. The methods may be categorized into one time measurement and continuous measurements. One of the most accurate measurement types is measuring the pressure differential across the Rotor Sail (RS). This allows an accurate representation of Pressure Coefficients (Cp) across the surface of the RS continuously, giving real time data and analytics on the performance. Similarly like in a wing profile this gives the basis to calculate Lift Coefficient (Cl) and Drag Coefficient (Cd). With this measurement methodology it is possible to actively monitor the propulsion created by RS . Strain Gauges give a really accurate representation of strain in structures; they are classified as highly accurate sensors. With strain gauges the deformation of object under load, such as the RS structure can be measured, giving also continuous real-time data and analytics of the RS performance. The main problem is that when mounted on the structure of RS, the gauges represent the moment created by the sail, not purely the lift force. Computational Fluid simulations (CFD) software can produce reasonably accurate simulations when supplied with appropriate reference conditions. The problem with CFD is that it simplifies some of the parameters, not fully reflecting actually accurate to the real-world conditions. [20] For these reasons, CFD serves as a valuable approximation tool rather than a definitive measurement method. As each simulation is computationally intensive and scenario-specific, CFD is classified here as a one-time measurement method. The On-Off method of propulsion calculation is a way where a ship keeps its course and main engine propulsion stable while the RS is switched on or off. The speed of the ship is measured with both states of RS, and a calculation is performed with known parameters such as hull resistance coefficient.

Method	Measurement type	timing	Accuracy	Advantages	Limitations
Pressure Sensors	Surface Pressure distribution (CP)	Continuous	Hight	Real-time Cl/Cd derivation across the rotor	Sensor placement, signal latency
Strain gauge	Structural deformation/moment	Continuous	High	Direct load data from structure	Measures lift indirectly
CFD Simulation	Computational flow model	One-time	Moderate	Flexible, no physical limitations	Very Simplified, computationally costly
On-Off	Ship speed differential in different RS states	One-Time	Variable	Captures pure installed performance	Hard to isolate Rs contribution from environmental noise

4.1 Pressure sensors

For reasons of confidentiality the name of the manufacturer and all relevant information that could identify the sensor type and producer are redacted from this thesis. All information about the sensor in parentheses "()" are indicative.

These sensors are miniature diaphragm-based transducers designed for measurement of pressure. Each sensor operates on the principle of diaphragm deflection under applied pressure. The diaphragm sensing element deforms in relation to the pressure difference on both sides of the diaphragm. This deformation is analogous to a spring, where its deformation x is related to the force acting upon the area of the diaphragm. With a known force and a known area, the pressure difference can be calculated. As the sensors deployed in RS system are measuring absolute pressure, the cavity behind the diaphragm is in a vacuum. Giving the sensor readings of absolute pressure. As the rotor rotates, pressure measurements are acquired all around the rotor. This configuration gives the ability to map out the whole pressure around the RS. As we know force might be derived from a pressure acting a surface area by $F = P * A$. By integrating the pressure distribution over the rotor surface the resultant force can be composed. This resultant is further broken down by creating two vectors in different directions. As per aerodynamical drag, this vector is directed in the same direction as the oncoming freestream velocity of air (Wind) and lift is perpendicular from drag. Accurate composition of these forces is important to operate RS system properly. Like conventional sail propulsion, made by canvas, drag can be useful should the wind direction allow usable drag component.

4.1.1 Manufacturer notes

As per the manufacturer notes of the sensor, a good overview is provided. The sensor appears well suited to a wide range of pressure sensing applications. As per the manufacturers handbook the sensor is built into a robust structure. It can withstand significant mechanical abuse without losing its calibration. Because the sensing is based on a miniature diaphragm which resistance changes according to the deformation of the diaphragm, changes in the sensing element are considered minimal. This is mostly thanks to the extremely small size, and mass of the sensing diaphragm. The notes mention the size to be "less than about" (<1mm)x(<1mm) and the low-pressure variant using a thickness of (<200 µm). The manufacturer also mentions that most of their pressure transducers can withstand at least (thousands of g) steady acceleration and (hundreds of g) peak acceleration, making a really robust sensor unit.

4.1.2 Possible errors in operation envelope

The operational envelope of these pressure transducers in the use cases of RS operations require the Sensor to be stable at a constant acceleration. This chapter presents an analytical assessment of the sensor specifications discussed above. The accelerations created by harmonic vibrations of the RS structure have been measured at the main bearing assembly (MBA) of RS which is located at approximately at 17m height of the 28m tall sail. The highest-pressure sensor is located at 26m height of the sail. This particular RS ,that serves as a testbed, has a strain gauge section with a height of 4m at the bottom. This section houses measuring equipment that will be discussed later. With vibration measurement from the height of the MBA, we can estimate vibration readings at the top of the sail. This will be done with a simplified rigid body approximation. Our given Peak values at a resonance RPM of the sail are measured to be $3.06\frac{m}{s^2}$. When interpolated to the top of the sail it would be $\frac{a_{mba}}{a_{top}} = \frac{h_{mba}}{h_{top}} \rightarrow a_{top} = \frac{a_{mba}*h_{top}}{h_{mba}} = 4.371\frac{m}{s^2}\ or\ 0.445g$. This measurement is taken before RS balancing, so it is considered the worst-case scenario.

In a worst-case scenario when vibration-based acceleration is in line with the centripetal acceleration, we can simply add these two together. The centripetal acceleration is simply calculated by $a_c = \frac{v^2}{r}$. V being the tangent velocity which is $v = \omega r$ where $\omega = 250rpm = 26.2\frac{rad}{s}$ and $r = 2m$ so $v = 52.4\ m/s$. From this we can derive the combined acceleration as $\frac{52.4^2}{2} + 4.37m/s^2\ = 1377.3m/s^2$ which is roughly 140g. With the g tolerance of the sensor error of (<<<0.01% /g) we can see that the sum error is miniscule. Error created by temperature in pressure readings is tenfold compared to this value so acceleration-based errors can be ignored. The temperature error is later corrected in the data data Acquisition system (DAQ).

Another thing to keep in mind is the acoustic harmonization of the sensor's cavity. As the pressure readings fluctuate at a constant speed, when RS is spinning at constant speed. This calculation can be simplified into a closed-open pipe, which resonates at $f_n = (2n-1) * \frac{c}{4L}$. As the highest frequency of the pressure changes (between high pressure and low-pressure sides of the RS) can be $\frac{250}{60} = 4.167\ Hz$. Using the resonance formula, we can determine what should be the minimum length of the cavity to reach resonance with the frequency of 4.167 Hz. Using $f = 1 * \frac{C}{4*L}$ where C is substituted with the speed of sound at sea level(341m/s). We can determine that $L = \frac{341}{4*4.167} = 18.8m$. With this information we can conclude that there is no possible way of the pressure sensors to achieve any sort of acoustic resonance.

4.2 Strain gauge

4.2.1 Working principle

A strain gauge works in a simple principle of resistance increase over mechanical strain. The sensor experiences a resistive increase in its conductive element as the element is stretched out. The sensor usually has a base made of flexible material on which the sensor itself is added. This gives the sensor the ability to stretch with minimal mechanical resistance, which is important to the proper adhesion of the sensor to a surface that is intended to be measured[21]. The sensor has printed or otherwise applied metallic foil cables that are designed to be stretched with accordance of the base plate. The resistance in that wire changes proportionally to the deformation of the sensor. This phenomenon is known as the piezoresistive effect [22]. This relationship is expressed by the standard formula for electrical resistance $R = \frac{\rho l}{a}$, where R stands for resistance, ρ stands for resistivity, l is the length and a is the average cross section of the object. The change in resistance comes from the change of the object's geometry. As the length is in the numerator, we can deduct that an increase in length will increase the resistance of the element, and as the average cross section is located in denominator, we can deduct that an increase in the average cross section will decrease the resistance. Typically, when an object is stretched out, both the length and the cross section is changed. The cross section will change with accordance of the Poisson's ratio which ranges from 0.06 to 0.30 with silicon [23]. To extrapolate resistance change in the sensor the sensing element usually resemblances the configuration illustrated Figure . This is done for a simple reason, of emulating a longer sensing unit into a smaller space. Using these methods a strain gauge can be designed, and it can be properly defined with the strain factor, which is $GF = \frac{\Delta R/R}{\epsilon}$, where ΔR is the change in resistance, R is resistance, and ε is the given strain. With this value every strain gauge is defined. By knowing the factor, resistance, and resistance change the strain can be calculated. Strain is a non-dimensional value that tells the difference in longitudinal length. So, the next question is how to measure accurately the resistive change in the sensor.

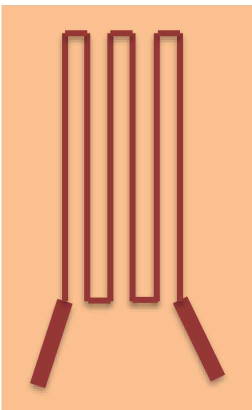

Figure 4: Figure of straingauge sensing element configuration

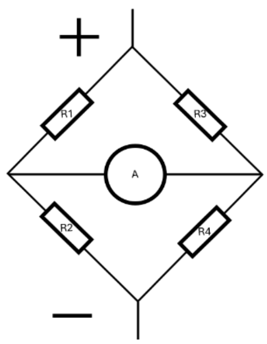

Figure 5 : Wheatstone bridge.

A Wheatstone bridge is an electronic device that can measure an unknown resistance with high precision. In the Figure 5 is shown how the bridge is built. When the Wheatstone bridge was first invented, it used an electro voltage meter instead of a galvanometer. It also had an adjustable resistance at R2. The resistance of R2 was adjusted until the voltage difference between both paths were 0. With the miniaturization of electron components, and for the sake of accurate long-distance data carrying this has been changed to more resemble the version in the Figure 5 : Wheatstone bridge.. It consists of four resistive elements arranged in two voltage divider branches: $R_1$and R_2form the left branch, $R_3$and R_4form the right branch. The output of the bridge is taken as the voltage difference between the midpoints of these branches. When the ratio of resistances in one branch matches the ratio in the other branch, the bridge is said to be balanced, and the output voltage is zero. Mathematically, this condition is expressed as

$$\frac{R_1}{R_2} = \frac{R_3}{R_4}$$

For example, consider a bridge supplied with 10 V and resistances $R_1 = 100\,\Omega$, $R_2 = 200\,\Omega$, and $R_3 = 150\,\Omega$. To find the nominal resistance of the strain gauge R_4that balances the bridge at zero strain, the balance condition can be used:

$$R_4 = \frac{R_3 \cdot R_2}{R_1} = \frac{150 \cdot 200}{100} = 300\,\Omega$$

When the strain gauge is at this nominal resistance, the bridge is balanced and no voltage appears across the midpoints. If strain or temperature changes R_4, the bridge becomes unbalanced, generating a voltage proportional to the resistance change. Measuring this voltage allows the applied strain to be inferred. The manufacturer of the sensor usually informs the sensors strain factor as it is important in decoding the data into useful information.

4.2.2 Possible errors in operation envelope

Temperature plays a key aspect in a strain gauge, as it affects various physical aspects. Materials tend to change size with temperature; this means that the folio wires that are used in a strain gauges differ in length because of thermal expansion. But not only the wires experience this effect, so does the base plate, which might be made of polymers, the adhesive, which is used to glue to baseplate into the structure, and the structure itself. As in this application, the strain gauge is used to measure strain created by mechanical forces, this is why it is important to distinguish between mechanical strain and strain caused by temperature difference. For this application the manufacturer of the sensor usually announces a coefficient that can be added to the measured value. This coefficient covers all the value distortions created by temperature in relation to temperature change. Another possible place for error is the mounting adhesive. This adhesive is responsible for conducting the strain of the measured construction onto the strain gauge. Usually, the manufacturer has a tested method of applying such an adhesive on different surfaces. The conduction of strain from the measured object into the sensor is an important step to affirm that the sensor readings are correct.

4.3 On-Off method

The following discussion is based on hypothetical values and is intended to illustrate the methodology conceptually. In this method the state of RS is switched between On and Off, while keeping the main engine power at a constant level. Using this method to calculate the propulsion of the sails is a clean evaluation of Flettner rotors, as with this method the effect is measured on a ship, not in simulation or as a standalone propulsion measuring method. With simulations and standalone tests, the propulsion of a RS can be calculated, but these calculations and measurements do not consider the height of RS, possible flow diversions from the hull etc. For this reason, shipowners usually prefer this data that is generated using this method, as the data is hard evidence with all the aspects integrated. While this method eliminates a lot of uncertain variables, it still has its own limitations. This method only works if the difference in ship performance can be unambiguously attributed to the RS performance. Accounted variables should be environmental, steering and main engine. Environmental deviations can only be minimised by averaging across multiple repeated tests conducted under similar atmospheric conditions. This is the only way to account for wind, wave and current changes. Ship trim and rudder position will vary during these tests.

Lift is rarely generated strictly forward, and its origin is seldom aligned with the vessel's centreline. Lift deviation from main engine propulsion vector will always create a moment in the system which will be trimmed out by a rudder input, or a rudder trim-tab input. When calculating fuel savings effect of RS this deviation is not a problem, as it would be included as an extra parasitic drag. But problems arise when calculating pure propulsion. The main engine thrust must be kept as a constant. An engine equipped with a fixed pitch propeller produces thrust inversely proportional to vessel speed. $T = \frac{P_S * \eta_p}{V}$ Where T= Thrust (N), Ps=Power at the shaft (W) and η is the propellers efficiency factor. Most modern vessels are capable of operating the main engine in a constant power output mode. Meaning that the main engine power output can be set as a constant in conducted tests. After this it is a simple equation of thrust to be sure that in this test the thrust will be kept at a constant state. As stated in the article written by V. Vigna and M. Figari [24] and other public sources[25] ship water resistance is usually only validated by small scale test conducting empiric, or semi-empiric validation methods.

This graph can be used to determine the net propulsion of auxiliary propulsion systems such as RS. While this example gives values of true thrust of the auxiliary system and simplifies some of the calculations necessary, it is difficult to keep all other variables constant during testing.

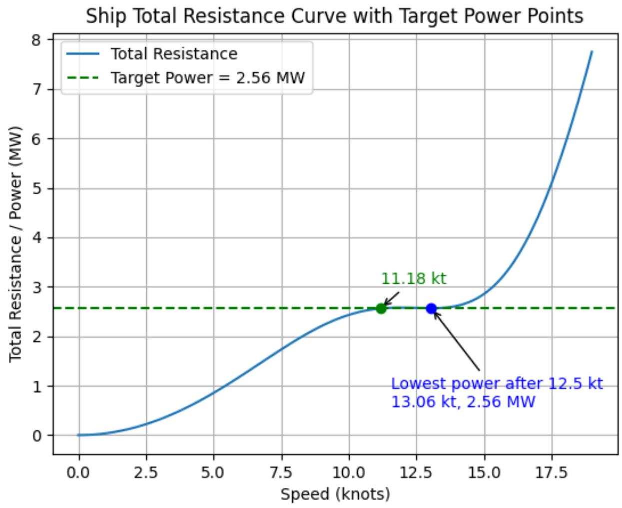

Figure 6: Fictional hull resistance graph.

A ship's hull drag chart is usually closely kept secret between shipbuilders. For shipowners there is a strong money incentive to buy a ship with the least total resistance. This hull would need the least amount of fuel to operate. As Fuel is a major operation cost it is wise to keep it small. A fictional hull drag graph was created to illustrate the point of the argument in Figure 6. This graph does not represent an actual physical measurement, but more likely represents the graphs that could be made by model tests. The graph in question is generated to illustrate what a ship's hull drag could be. The form resembles other fictional graphs found in [25], [26]. This graph represents total resistance. Meaning that the figure has included resistance created by viscosity, wind, wave generation and others. As you can see, the graph has a peak at 11.88kt. This is considered the hulls hump speed. It is created by open surface wave dynamics. At speeds approaching a hull's hump speed, a displacement ship experiences a sharp rise in total resistance due to wave-making effects. This increase arises from constructive interference between the bow and stern wave systems, which amplifies wave height and energy loss. As vessel speed increases, the dominant wave wavelength grows until it becomes comparable to the ship's waterline length, causing the hull to be constrained between its own generated waves and significantly increasing wave-making resistance. This occurs because the vessel must expend additional energy to overcome the waves it produces, particularly when the wavelength of these waves approaches the ship's waterline length. In this regime, the ship effectively "rides in a trough" formed between its own bow and stern waves, resulting in a nonlinear increase in resistance for incremental speed gains.

When comparing the change in speed created by RS it is important that accurate total resistance curve is known. For example, let's have our hypothetical ship sail at exactly 2.56 MW of main engine power. This means that on the graph there are two possible speeds the ship could sail. Let's say that the ship was powered over the hump to its higher possible speed. At this speed, the ship uses 2.56MW of NET propulsion. After turning the RS system on and off, for the sake of the argument let's say the conditions are ideal, the speed increases to 16.1kt. From this graph we can see that the power requirement will rise quite sharply. At 16.1kt the power requirement is roughly 3.49 MW. This means that the RS created a 0.9MW of propulsion.

This has been a fictional example of how to calculate the propulsion production of the RS system with a hypothetical value, to illustrate the On-Off methodology. The corresponding fuel savings can be calculated from this figure. As reported by the United States Naval Academy [26], the ships engine can produce engine power at 40% efficiency compared to the fuel energy. The engine produces net propulsion at 24% efficiency, once the drivetrain, gearbox and propeller efficiency coefficients are added to the calculation. This means that the engine has to always work at $\frac{40}{24} = 166.7\%$ workload compared to the net propulsion. So, in this hypothetical scenario the RS system can save up to $1.667 * 0.9MW = 1.5MW$ of the ships main engine power. If inspecting a best-case scenario, the RS can produce 30 times the amount of propulsion compared to the power consumption of the system, we get $\frac{0.9MW}{30} = 30\ kW$. So, the net power profit from this scenario will be 1 470 kW, completely harnessed from the wind. Another way to look at this is that the vessel speed can be brought up from 7.3kt to 12.5kt by just using 30kW of energy for wind propulsion. But this only illustrates the hypothetical best-case scenario, which is based on reported values and aims only to explain the concept of On-Off measurements. As stated earlier some of the values used in this scenario are tightly kept secrets and thus any real data on this experiment cannot be published.

5 Research methods

This thesis evaluates the propulsion measurement and estimation methods applicable to Flettner Rotors and validates the reliability of the pressure-sensor-based system deployed on Norsepower RotorSails through experimental testing and CFD comparison. This thesis uses two approaches to answer the three research questions. The first approach uses a qualitative literature review, while the other uses quantitative data-driven validation. Together these approaches give the reader both the technical background and the theoretical foundation to validate the data and shown conclusions.

The first segment addresses the first question with a comprehensive literature review. The literature review covers the historical development, theoretical principles and current state of Flettner Rotors. As covered in the earlier segment the technology has been around for over a century, consequently the sources span over that same time, including pre- informational era publications based on physical measurements of miniature and full-scale models of Flettner rotors. For proper numerical studies more current sources from the digital era have been included for better CFD simulation data. This broad scope of sources is intentional, as it best reflects the technology's full arc of knowledge and development and helps identify why full-scale adaptation has historically been limited despite the well proven concept.

The second segment includes a study that answers questions 2 and 3. This segment has a quantitative study in which propulsion measurements for Norsepower test site Rotor Sail are compared with CFD simulations and alternative measuring methods. Three tests were designed as part of this study, of which two were ultimately conducted:

1. Test1, emulating a pressure sensor signal.
2. Test2, Examining any phase change in the pressure matrix (left for further studies)
3. Test3, compares the result across all measurement methods using real wind test data collected on 8.4.2026

The result and methodology of each test are presented at the start of their respective chapters. The aim of these three tests is to validate the propulsion measurement approach. Data is drawn from RS DAQ

Artificial Intelligence tools were utilized in this thesis, primarily to assist the study of test data and visualizing said data into an understandable format. Python scripts were developed and iteratively refined by AI to achieve the wanted tools for visualizing and analysing the data. The tools only function was to create visualisation of the data, and the interpretation and validation of these scripts was done by the author. Using AI in this function gave a significant practical advantage by reducing the time required to produce functional analysis tools and gave the opportunity to completely build up the tools needed to produce exactly the wanted outcome. The use of AI was considered appropriate due to the aim of this study being more analytical and less focused on studying how to create the tools.

6 Digital Tools in data analysis

This chapter provides a detailed description of the digital analysis tools employed in the experimental part of this thesis. The Fast Fourier Transform (FFT) algorithm is an efficient method for computing the Discrete Fourier Transform (DFT), which is the discrete counterpart of the continuous Fourier transform. The DFT operates on sampled and finite-length signals, representing them as a sequence of discrete time-domain values. The classical Fourier transform is usually defined as $F(\omega) = \int f(t)e^{-i\omega t}dt$. This function can break down the signal in the time domain and reveals resonating signals. In essence it projects the signal onto cyclical basis and measures how much of each frequency is present. This transform is defined for infinite signals, and even though it can be applied on finite signal, it is not the best algorithm to use when studying finite signal or windowed signal. These elements bring problems such as spectral leakage into the composition.
When studying a sampled measuring data, such as a database with time and value variables, x[n] a non-continuing signal wave it is important to use Discrete Fourier transform. This is determined with $X[k] = \sum_{n=0}^{N-1} x[n]e^{-\frac{i2\pi kn}{N}}$ and represents a finite number of frequency bins. A frequency bin tells the amplitude of signal at that bin's frequency.

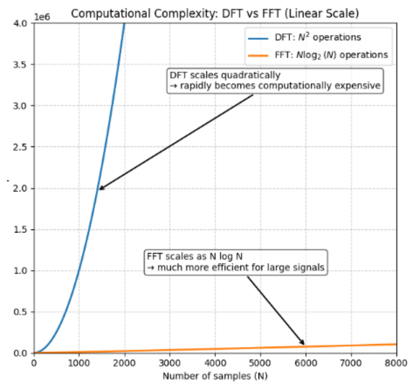

Figure 7: FFT vs DFT computational time.

The FFT is a class of algorithms that computes the DFT with substantially reduced computational complexity [27]. FFT is widely applied across engineering sectors, from communication systems to audio processing and vibration analysis, where signals must be analysed in the frequency domain. Due to its computational efficiency, FFT is one of the most important algorithms in modern digital signal processing. Over the years, multiple FFT variants and optimizations have been developed. In this thesis, the FFT implementation provided by the NumPy library is used. The key advantage of FFT compared to DFT is that it can reduce the computational load of the algorithm. FFT can process the data in $O(N\ logN)$ instead of the DFT $O(N^2)$ which is visually demonstrated in Figure 7. As seen from the figure the FFT requires a lot less computational operations (y-axis) compared to the DFT. The presented reasons illustrate the computational advantage of the FFT over conventional DFT.

NumPy computes the DFT using an optimized FFT algorithm and returns a discrete set of frequency bins. Each frequency bin represents the contribution of a specific frequency to the original time-domain signal. The spacing between these bins is determined by the sampling rate and the length of the analysed signal.

Another algorithm used in this thesis when inspecting signal is Hann windowing, or Hanning[28], [29]. The purpose of this window function is to reduce spectral leakage when computing signal data with FFT on finite data length. Spectral leakage occurs because FFT assumes that the analysed signal segment occurs periodically, when in practice the measurements are finite. Measured signals do not begin and end at the same phase of signal, which creates a discontinuities data at the boundaries of windowing. This discontinuity introduces additional frequency components that do not exist in the data. The Hann window mitigates this effect by smoothly bringing the amplitude of the signal towards the median, or zero, at both ends of the sample. This mitigates the abrupt discontinuities of the samples, achieving a clearer FFT spectral analysis of the signal.

7 Conducted test.

The objective of this part of the thesis is to validate the data that Norsepower DAQ records and calculates. The scope of this thesis is to understand the data that the DAQ record and validate it partially, as full validation did not fit the time schedule. Reports created on earlier measurement data (NATE vs CFD 23-02-2026 JVo) show that at the company test site located in Naantali, Finland, the actual Lift created by the RS does not correspond with CFD simulations. A difference of ~ -10% in CFD simulations has been observed, meaning that measured data seems to be higher than simulated. Up to this point this has been explained by CFD simulation inaccuracy. To challenge this outcome two hypothesis have been created.

1: The measured pressures are inaccurate due to DAQ.

a. A latency in pressure readings at full RPM will create a phase shift of the pressure matrix, which is a map of known pressure values at a known location on the RS.

b. Sensor signal quality is not clean, creating anomalies in the data and further disrupting data integrity and calculations.

2: Inaccurate pressure readings create inaccurate calculated data.

a. When calculations are made on inflicted data said calculations show a trend that does not correlate with expected results.

b. Tighter filters on test runs gathering data would reduce the current difference of measured and simulated data (10% to 12%).

7.1 Test 1, pressure sensors emulation

In this test the sensor reading system will be tested with a pulse generator. This test will aim for resolving hypothesis 1b. In this test a pulse generator setup will be used in order to emulate a signal that is similar to the pressure sensor. The sensor in use is a type of diaphragm that is connected to a strain gauge. On one side of the diaphragm is a known pressure, which does not change. The manufacturer specifies that the sensor is robust and the pressure chamber does not leak or have any change in its containing pressure during the sensor's lifespan. The sensor's measuring range is between 68 948 Pa and 124 106Pa (10 to 18 psi). The output signal of the sensor is 4mA and 20mA respectively to the pressure ranges. The data acquisition system (DAQ) responsible for pressure-based force vector calculation has the following components:

1. Pressure sensor card.
    a. This card reads the pressure sensor value at the frequency of 1kHz and stores it into a readable format.
2. The main software
    a. This software reads pressure of the card at 1kHz and sends this data to the propulsion software.
3. Propulsion software
    a. This software creates a map of pressures for each sensor. It then assumes that the pressure is the same for a 1m height segment of the rotor, and with that area it calculates the force created by the Magnus effect.

The aim of this test is to read the recorded data and compare it to the pure signal (wavefront.bin) data and see if there might be any possible deviances to the wanted values. For this reason, it is important to note all failure points of the test setup as well. The test setup consists of:

1. Pulse generator
    a. This generator is type OWON AG 10112 F. This generator can create any type of waveform with a maximum amplitude of 10v.
2. Voltage to Current (V to C) converter.
    a. When applying any sort of load to the pulse generator its power was not sufficient to generate any current. This sort of chip was integrated into the test setup to create a signal of current directly proportional to the voltage signal. V to C converter uses another power source to power the signal
3. 9v battery
    a. This battery was used to power the V to C converter. To have consistent result, a fresh 9v battery was always used on each test day.

Assumptions:

- The generator is a widely used laboratory instrument, and the manufacturer specifies an accuracy of 1 mV and 1 μHz. -> generated pulse is accurate
- All test setup power cables (230Vac) were setup to be as far away as possible. -> **no interference in the additional test setup**
- V to C converter accuracy unclear. Manufacturer promises precision of 1mA. The output current was precisely measured with ammeter and tuned with potentiometers (see. Figure

8) integrated into the chip. A test was run to see that the amperage does not deviate from set values, test was successful. -> **V to C converter accurate.**

- As the chip produces a miniscule current, the Wattage is small (<0.2W). No manufacturer mention of chip power usage for other operations than output. Assuming chip complete usage at max =0.5W -> 56mA. As battery has 614 mAh [30] and usage per battery is assumed to be 56mA for max 25min this means usage of 23 mAh (under 4% of capacity) -> **Power source voltage stable**

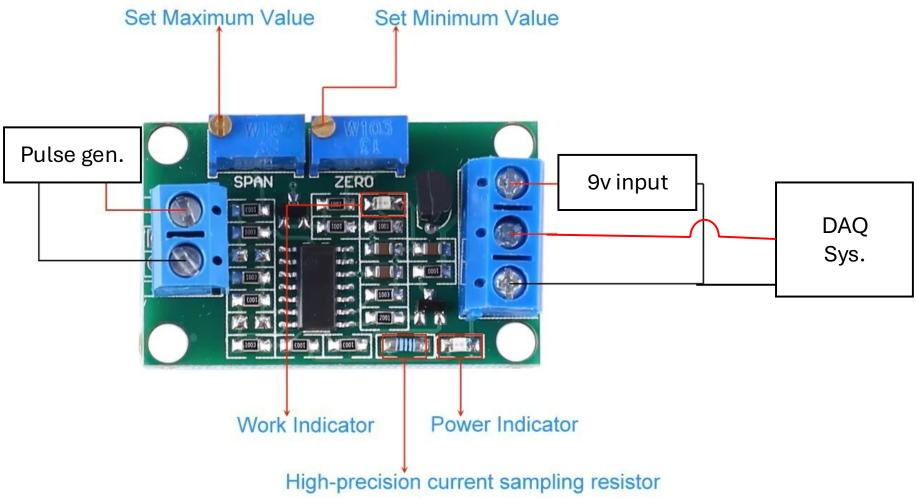

Figure 8: Test setup chart

7.1.1 Test results

For this experiment an arbitrary waveform was generated. For the generation a script called waveform_gen_csv_bin.py [31] was created. This script generates a wave with 4 different periods. The first period is a wait period. During this period the waveform does not send any signal out. See Figure bottom middle plot "Should resemble" for reference. This period was created to give a clear reference point in the data when observing signal later in data analysis. It proved to be very useful and a reliable reference point later on. This period lasts for 1/16 of the length of the waveform. This period is followed by a square wave for 5/16 of the whole wavefront length. The aim for this signal was to have an easier reference to work with compared to sine wave. The square wave has extremely steep walls and switches instantly between the minimum and maximum. This should show the system's ability to record data with major changes. The square wave segment also proved to be extremely useful later on. The third period is regular Sin-wave, which emulates the most common signal from the pressure sensor in perfect form. The sine-wave period is also 5/16 of the length. The final period has 7 randomly picked sinewaves combined to create a fast but continually changing signal. This period aims to simulate “sound” in the signal and lasts 5/16 of the length. The script generates two files, one is a .bin file that has the proper footers for the OWON pulse generator to read and the other contains the same information in .csv. The header had to be reverse engineered from a valid owon.bin file, as any information was not found online. The header included data such as filetype, vertical sample time base and total number of samples. In the process of reverse engineering the generated file was accepted by the pulse generator, and it was able to output it. But for some reason the generator was not able to visualize the pulse on the screen of the device. Nonetheless the signal that the generator created was correct. The other file that the script generates was a .scv file. It is important to generate both at the same time as the script has random elements. The waveform is discretised into a fixed number of points (8192) which are then converted into 16-bit integer format matching the requirements. The wiring diagram can be found in Figure 8.

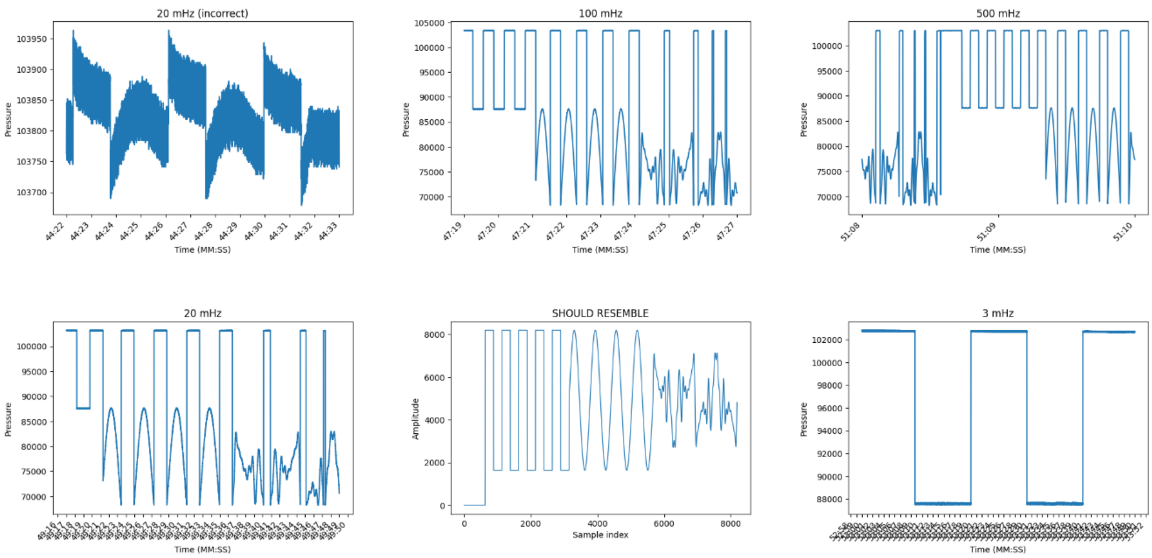

Figure 9: First test-run (incorrect setup @20Hz)

After the first test (7.1.2 Test logs, 25.4.2026) it was time to download the data from DAQ and process it. The downloaded data comes in a csv file with one row per second. In each row there are 1000 comma separated values for each millisecond. This is due to data collection being at 1kHz. To validate the data a python script counter.py [31] was used. This script counts every row and its values. After verifying that each row has 1000 values it prints out the result. Some rows, seemingly at random had lost their values returning 0 values per second. This data loss was at random, and it was good knowledge when taking the next step. CSV_opener.py [31]script was made to rename each time stamp and open the rows. Now there would be a new .csv file named xxxx_opened.csv with each row having a precise timestamp to the millisecond with one value. This made it easier to plot said value. For plotting a script named EMULATE_PLOT.py[31] was created for visualizing the data. The script reads the data at known time interval. This time interval was logged in the test log. This way a single file may contain all the test from one day and the plot can pick the timeframe from which it plots. The frequency indicates how many times the WHOLE waveform was sent out. So, at one Hz the whole wave with multiple signal peaks would be sent each second, the frequency is not to be confused with each square, sine or random wave. To get better flexibility in visualizing the data the script has a parameter to indicate from which second the plotting should start, and how many seconds should be plotted. At every frequency each wave is different in length.

Through this analysis several key observations were made. The readings downloaded from the DAQ showed anomalies at the lower end of signal amplitude. This same anomaly can be seen in every correctly executed test. This indicates to a malfunction or a systematic error of the test setup. As the DAQ is designed to only sense readings between 4mA and 20mA, which correlates to the pressure sensors minimum and maximum, it may be concluded that signal loss occurs when the current falls below the 4 mA lower threshold of the DAQ input range, as the highpoints seem to correlate with the wanted wave. The hypothesis is that when the current drops below 4mA the reader card "loses" signal and the recorded data loses its values. See plot at Figure . As mentioned before the 20mHz (Incorrect) had an incorrect test setup and this is why it was unusable. Otherwise, the other plots show the signal quite clearly.

Upon trying to retrieve the data from the DAQ after this test (7.1.2Test logs, Test day 27.4.26), it was noticed that during the earlier week the DAQ Main PLC had been in a fault state due to an incorrect software update. This meant no data was recorded. A repeated test was conducted once the recording fault had been solved, and the main PLC had been restored to normal operation. This was done the next day (7.1.2 Test logs, Test day 28.4.26). By running the data through counter.py[31] it seems that three rows have lost data.

```
Row 18 (Column B) | Timestamp: 2026-04-28 14:30:17+00:00 | EMPTY
Row 38 (Column B) | Timestamp: 2026-04-28 14:30:37+00:00 | EMPTY
Row 56 (Column B) | Timestamp: 2026-04-28 14:30:55+00:00 | EMPTY
Total problematic rows: 3
  - Empty rows: 3
  - Wrong value count rows: 0
```

As every test duration is 1 min luckily these data losses are in between tests and do not affect results. Next up we run the script CVS_opener.py[31] to open the data. After plotting the opened data, it is clear that the same problem persists (Figure 10). This time it was surprising as with the ammeter in the test setup loop the values displayed showed to be correct. This has probably something to do with the test setup not being completely compatible with the DAQ. Nonetheless, the square wave did come as clean signal and from now on only it will be used in analysis. As from the plot named "should resemble" in Figure 10 we can see what type of signal was sent to the DAQ. In this signal we can see that the first segment with the square waves is sent out to emulate the pressure sensor. Before the first segment a 0mAh signal is sent, this signal is shown as a maximum in the plots, also the sine wave tops are for some reason a lot lower than the square wave tops. This would indicate that the problem is in the test setup and the small converter chip cannot produce the wanted signal. On the test day current was measured during signal generation, and currents of 5.5mA and 15.3mA were shown. This should be still in the range of the DAQ. For this reason, it was deemed OK to use this data to study the signal quality

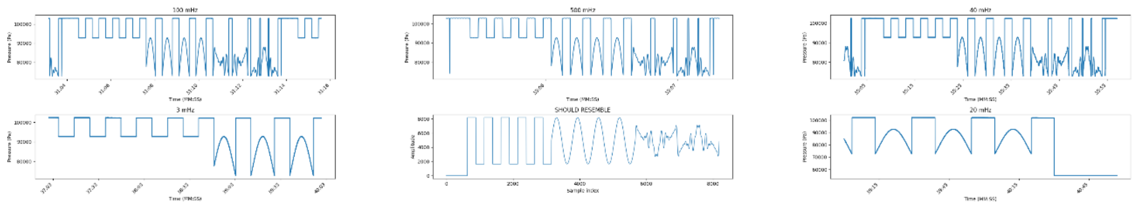

Figure 10: Second test-run

The next script will focus on the square wave segments, as they are the only ones that the test setup got to work. For starters let's just investigate one of those segments at each frequency, like illustrated in Figure   to Figure. The frequency is marked for the whole arbitrary wave, not just every wave like usually. As the frequency increases the datapoints on the square wave decrease, this will decrease the accuracy of the upcoming analysis as frequency rises. The working idea on pmit_sound_plot.py [31]script is to isolate the wanted segments and plot them. After this an ideal reference wave is plotted on top using a threshold classification method. A threshold is set to the average of the waveform, and an average on both sides of the threshold is calculated. The average is calculated for values above and below this threshold. These two averages then dictate the high and low values of the square wave. Every sample is assigned either the high or the low mean value depending on which side they are placed on the threshold. This creates an ideal square wave. The residual, defined as the difference between the measurements and the ideal wave, isolates all deviation found in the signal wave

from the ideal wave. This deviation includes all the environmental interference the DAQ inherits. A known limitation of this system is that actual pressure does not jump from one pressure value to another in under 1ms. When plotting the data it was observed that these switching edges did produce large spikes in the residual wave pattern that were orders of magnitude larger than the background noise of interest. A solution for this problem was added to the script in form of a mask that "cuts out" these spikes. As these spikes would prove problematic later. These masks can be seen on the plot to make it more visually obvious of their working principle. The output of the code:
Console output:

```
100 mHz:
  Samples             : 1860
  High avg            : 103057.716 Pa
  Low avg             : 92718.704 Pa
  Amplitude           : 10339.012 Pa
  Threshold           : 97921.561 Pa
  Residual RMS (clean) : 48.037 Pa
  Dominant noise freq : 50.9868 Hz

500 mHz:
  Samples             : 367
  High avg            : 102762.211 Pa
  Low avg             : 92701.797 Pa
  Amplitude           : 10060.414 Pa
  Threshold           : 97759.380 Pa
  Residual RMS (clean) : 57.461 Pa
  Dominant noise freq  : 54.3807 Hz

40 mHz:
  Samples             : 9378
  High avg            : 102561.139 Pa
  Low avg             : 92713.225 Pa
  Amplitude           : 9847.914 Pa
  Threshold           : 97743.691 Pa
  Residual RMS (clean) : 46.669 Pa
  Dominant noise freq  : 50.2034 Hz

3 mHz:
  Samples             : 51283
  High avg            : 102269.593 Pa
  Low avg             : 92709.102 Pa
  Amplitude           : 9560.491 Pa
  Threshold            96669.244 Pa
  Residual RMS (clean) : 51.304 Pa
  Dominant noise freq  : 50.0312 Hz
```

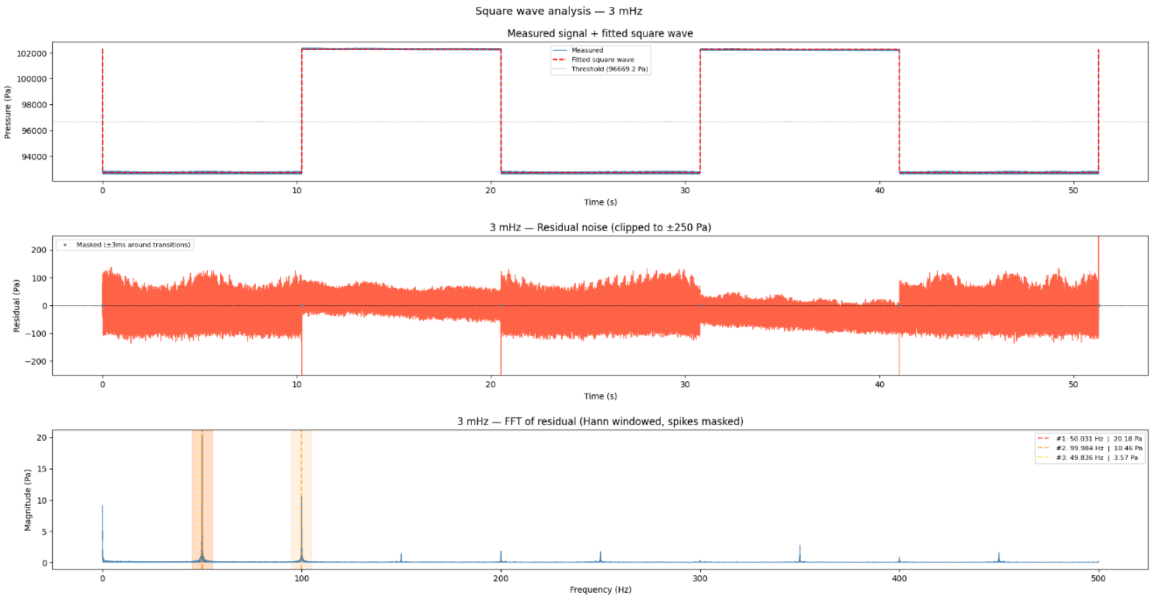

Figure 11: Spectral analysis of 3mHz

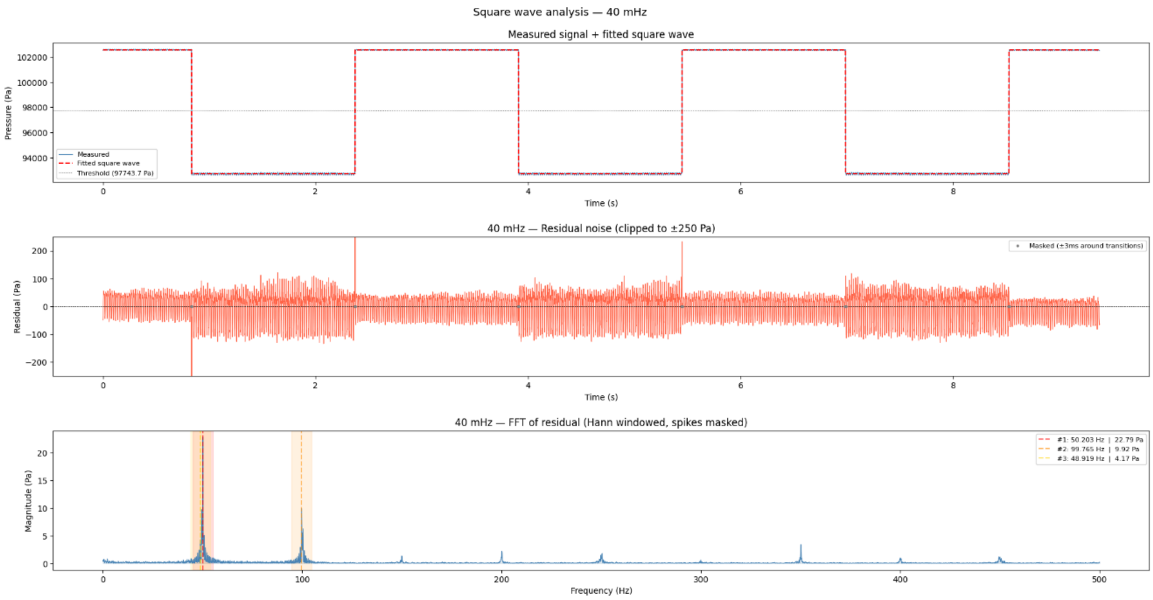

Figure 12: Spectral analysis of 40mHz.

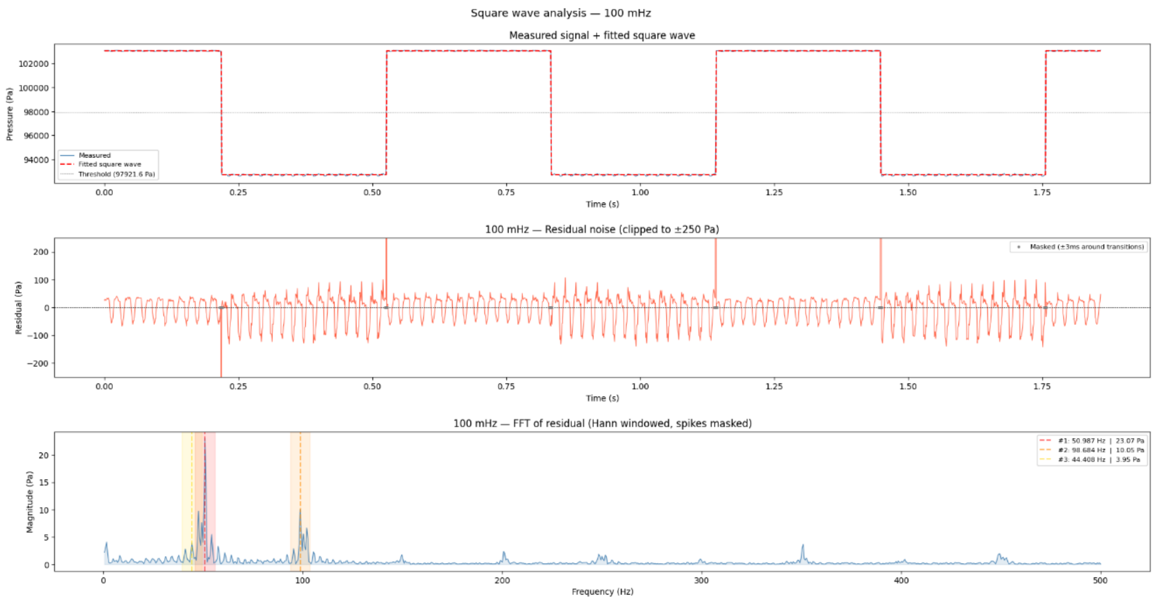

Figure 13: Spectral analysis of 100mHz

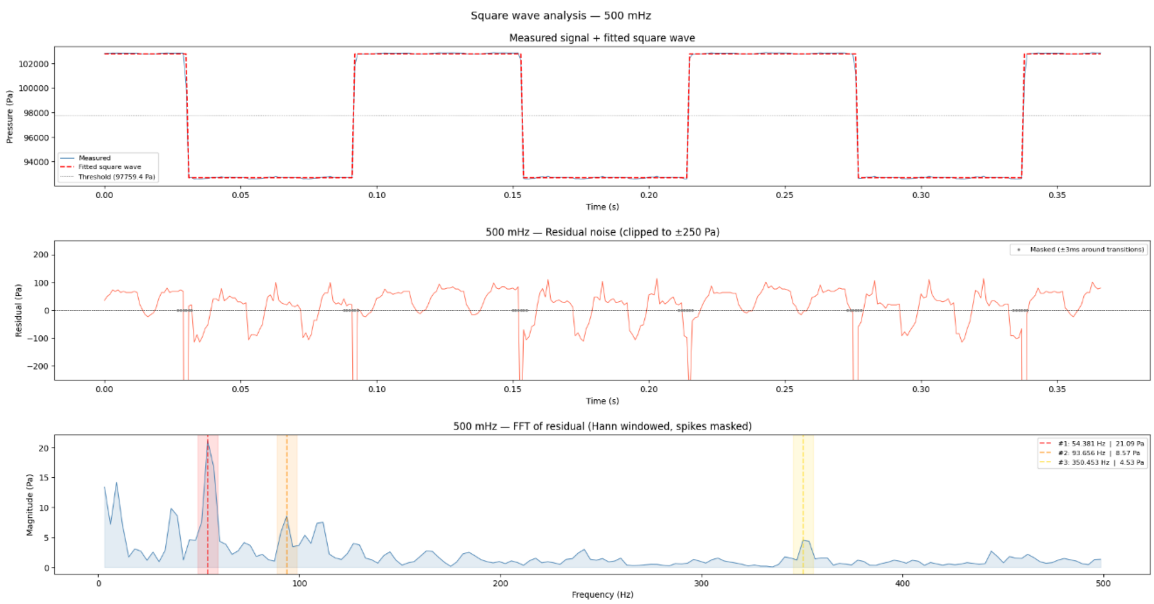

Figure 14: Spectral analysis of 500mHz

When observing the residual wave, it was clear that the sound recorded was cyclical. For this discovery a Spectral analysis of the cleaned residual wave was created using Fast Fourier Transform (FFT)[32], [33], which breaks down the time-domain noise signal into its constituent frequency components and the reveals whether any systematic interference is precent. A known artifact of applying the FFT to a finite data segment is spectral leakage: because the FFT mathematically assumes the input signal repeats infinitely, any mismatch between the amplitude at the start and end of the window creates an artificial discontinuity that spreads energy from real spectral peaks into adjacent frequency bins, producing a characteristic sin-function ripple across the spectrum. To suppress this effect, a Hann window function is applied to the masked residual before computing the FFT [28], [29]. The Hann window tapers the signal smoothly to zero at both ends, eliminating the boundary discontinuity and significantly sharpening the spectral peaks. The magnitude of the FFT output is corrected for the amplitude reduction introduced by the windowing function by dividing by half the window length, restoring physically meaningful units of Pascals. The dominant frequency is identified as the bin that has collected the most values and is marked on the plot, as well the amplitude.

The script (pmit_sound_plot.py [31]) produces one independent figure per test frequency, each containing three vertically stacked subplots. The first subplot overlays the raw signal and the fitted ideal square wave. The second sublot shows residual noise with the y-axis clipped in order to better illustrate the wanted residual wave. In this subplot it can be visually confirmed that the difference in datapoint number creates a difference in the data across all the tested frequencies. The third subplot shows a Hann-windowed FFT magnitude spectrum of the masked residual. All figures are rendered simultaneously in non-blocking mode to give better chance to compare the plots. A console summary is also printed for each frequency, reporting the number of samples, mean high and low pressures, total pressure amplitude, classification threshold, root-mean-square residual of the clean signal, and dominant noise frequency. With this visual and numerical output, the data can be observed.

After observing that there is major interference in the data, as high as 20 Pa at 50 Hz, the test setup is put to question. Interference of 20Pa should be visible in normal operation of the sail and with CFD simulations showing that ΔP in operations should be around 390Pa(Figure 15), 20Pa would have a 5% amplitude uncertainty. This sort of error would have been seen in data gathered during operations, where the measurement equipment was unaffected. While this does not disprove of the presence of 50Hz interference, the magnitude of the amplitude does raise questions. After this discovery testing continued while trying to eliminate all possible interference sources one by one. After every test the scripts were ran again to see the spectral analysis and observed if the problem persisted. To isolate the interference source a systematic elimination procedure was conducted, progressively removing each component or possible interference source from the setup. After re positioning and shortening the cables, with the aim of create as little of proximity to the mains power, the issue persisted. The next step was to remove every other component rather than the pulse generator or the V to C converter. The issue still was not eliminated. As the V to C converter was powered by chemical battery as its power source, a deduction was made that the only possible source of 50Hz was the pulse generator, which itself was powered by 230V 50Hz ac. It seems that the assumption of laboratory equipment accuracy was indeed incorrect.

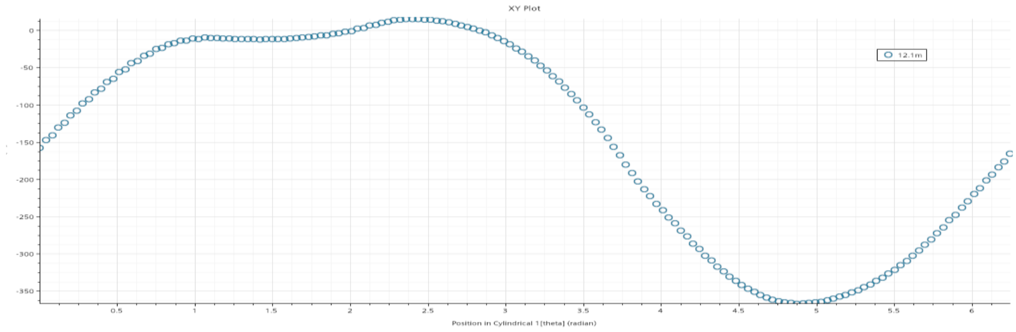

Figure 15: CFD Pressure measurements.

As with the emulated pulse the DAQ gets pressure values between 103057.716 Pa and 92718.704 Pa (taken from 100mHz test), creating a gap of 10 339.012 Pa. This gap is measured when pulse generator voltage goes from its supported maximum (10v) and minimum (0v) voltage. This means that 20 Pa is ~0.193% of the signal range. This sort of error is quite low, and the manufacturer promises a margin of <1%. Which means that the used equipment was NOT sufficiently accurate enough for this test.

As a final trial a new script was created. The script pmit_sound_plot_2.py [31]was heavily based on the original pmit_sound_plot.py[31]. This code takes two different pressure sensor values at the same time of the conducted test. One is Press1 and the second is Press5. The idea of this script is to plot the values for easy comparison of an emulated channel and clear sensor signal. These plots can be seen in Figure and Figure 17. From this we can deduct that the actual signal is being affected by 230V 50Hz ac, but the actual amplitude is only 1.65 Pa, which in the scale of measuring range is under 0.38% of error. The occurrence of 50Hz interference in Press 1 channel and its nonexistence in Press5 channel, which was not hooked up to the testing setup, further proves that the experienced interference was due to the test setup itself. This method provides proof that the measuring still suffers from 50Hz interference, but at much lower magnitude than firstly discovered.

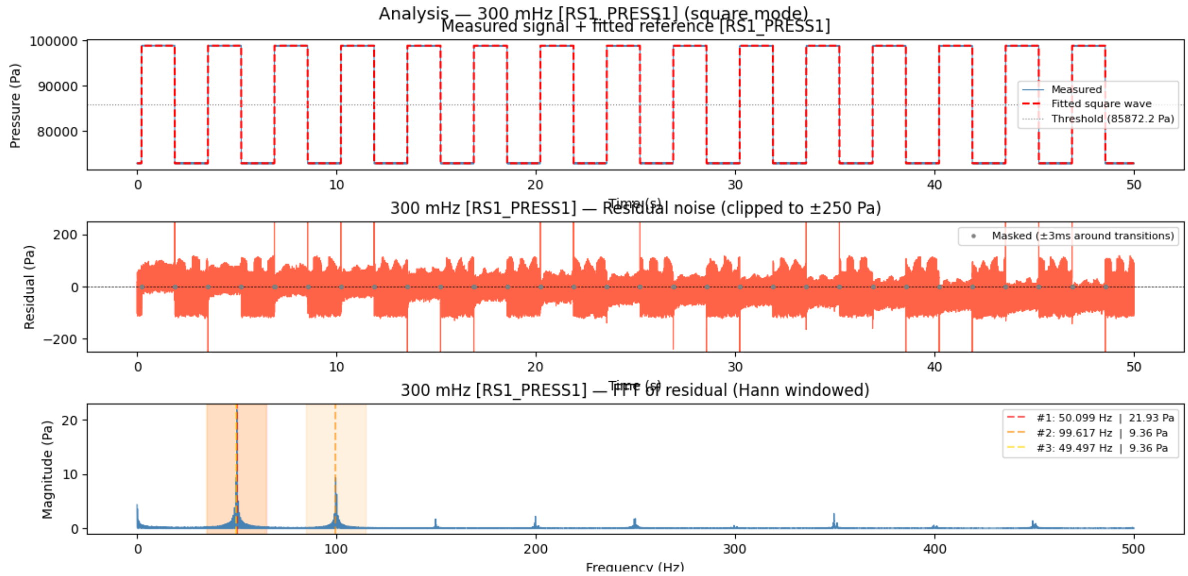

Figure 16:Sensor1 emulated signal

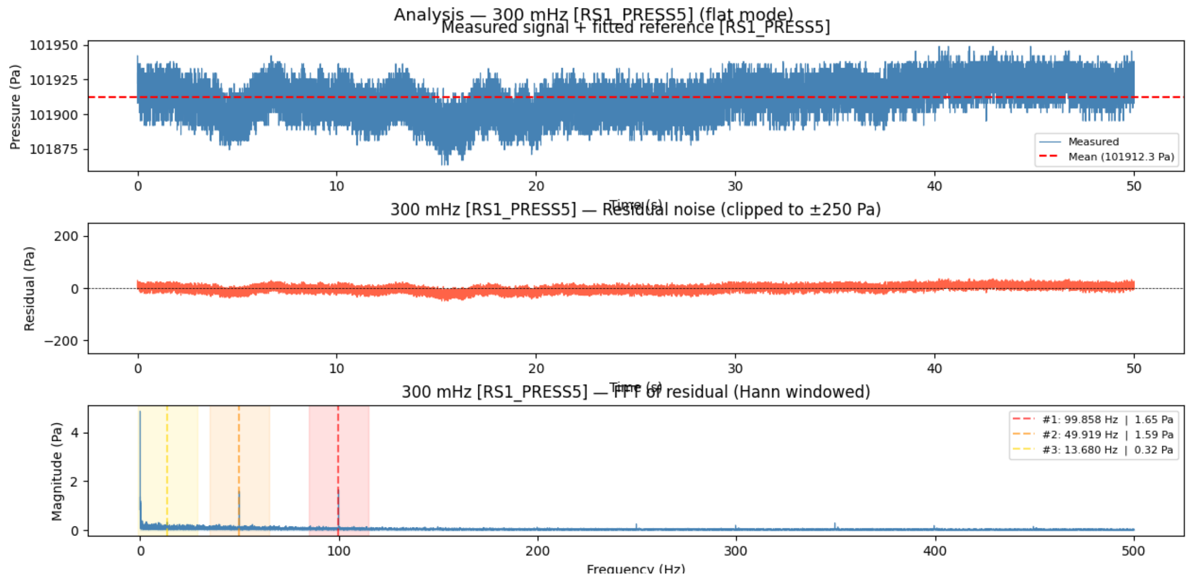

Figure 17: Sensor 5 (raw sensor signal)

7.1.2 Test logs

Test day 25.4.2026

Maximum value 19.2mA
Minimum value 5.2mA
Start time 13:41

13:42 Loaded successfully OWON9876.BIN
13:44:00 1min signal at 20 mHz
13:46 settings were not correct. Inputting correct values and trying again
13:47:00 1min signal at 100 mHz
13:49:00 1min signal at 20 mHz
13:51:00 1min signal at 500 mHz
13:53:00 1min signal at 3 mHz (20sec over)
test end

Pressure sensor test 27.04.2026.

11:58 test start.
11:59 test square wave duty cycle 50% 100mHz amplitude 5mA – 14.1mA. Test setup current goes through ammeter for better understanding of data; with added load the signal cannot reach higher than 14.1mA. This should not be a problem only the data up to 14.1mA will be used.
12:01 test with arbitrary waveform 100mHz.
12:08 test end
12:10 arb wave 30 mHz for 1min.
Test end

Test day 28.4.26

Start time (UTC+3): 17:05, Time logs in UTC.
14.08 square wave 1min 2hz and 0.5hz. Checking if setup is correct.
14:26. Run through CSV_opener.py and Emulate_plot.py. Clear square wave is found. Next up, arbitrary waveform test
14:29 maximum 15.3mA minimum 5.5 mA with square wave form. So 10v and 0v
14:31 arbitrary 100 mHz
14:33 arbitrary 500mHz
14:35 arbitrary 40 mHz
14:37 arbitrary 20mHz
14:39 arbitrary 3 mHz for 3 min
14:42 test end

7.2 Test 2: Pressure matrix phase change (proposed)

This test is designed to determine whether any phase shift occurs between the actual sensor position and the recorded position during data acquisition. Both this, and

Test 1, pressure sensors emulation are aimed to answer RQ2. To test this a pressure will be applied to a known sensor in a known position. To maximise the visibility and detection of the error, the RS should be spun at the highest feasible rotational speed. As this will create the largest latency-based phase change. High rpm will create a lot of lift which is why the test should be done on a calm day. To apply pressure to a spinning rotor an aerial work platform (AWP), or any other standalone system should be used. This system would bring a pneumatic pistol, connected to a pressurized air tank, near the sensor. Whenever the sensor passes over the high-pressure area the spike would be recorded in the DAQ system. The hypothesis is that should the system have any lag, the pressure matrix will have a spin ward phase shift. Here is the structure of DAQ that is responsible of measuring the pressure matrix.

1. Encoder card.
    a. This card reads the encoder at a frequency of tens of kHz with an accuracy of $\frac{\pi}{2000}$RAD to deduce the position of the sensor.
2. Pressure sensor card.
    a. This card reads the pressure sensor value at the frequency of 1kHz.
3. The main software
    a. This software reads this position and pressure for both cards at 1kHz and sends this data to the propulsion software.
4. Propulsion software
    a. This software gets the location of the pressure and the pressure value at 1kHz. An array is created giving a pressure value sequence of the whole spin at a known height of the rotor. Should there be any lag, or differentiating lag, during this writing, the mapping might be created with a phase change.

7.2.1 Possible occurring errors.

As the rotor is 4m in diameter, the circumference is $\pi * 4m = 12.566m$. The resolution of the encoder is $\frac{1}{4000} * 360° = 0.09$ °. The main software divides the surface into 250 sectors for pressure measurement. $\frac{360°}{250} = 1.44°$. Just on software alone the measuring has an accuracy sector of $\pm 1.53°$ which corresponds to a measure of $\frac{1.53°}{360°} * \pi * 4$ =53.76mm across the surface of RS. At the speed of 200 RPM the surface velocity is $\frac{200rpm}{60s} * 12.566 = 41.9m/s$. This means that to travel 53.75mm the surface takes $\frac{0.05376}{41.9} = 1.28$ms. So, in theory a latency that is >than 1.28ms could lead to a phase change. The Determination of the position of the spike will be done when the RS is stationary. This will enable the usage of the same equipment in determining the change in the spike location. Should any errors occur in the measurement, they would be cancelled out by themselves.

Assumptions:

- When using RS DAQ for both control parameters and test run all possible errors cancel out.

At the time of writing this thesis, this test was abandoned owing to safety constraints and scheduling limitations. The proposed method required aerial work platform access to a spinning rotor, which introduced safety constraints that could not be solved in the timeframe. Nonetheless the Author of this thesis suggests further testing to verify this latency issue. For the purpose of Test 1 and 3, an assumption is made that there is no phase change in the pressure matrix as this tests results would not affect the methodology of other tests.

7.3 Test 3, comparing all data across all measuring methods.

This test will be performed on a windy day, hence it is named windy_day_test in filing. Seeing the topology near the test site (Figure 18) the most favorable wind directions are picked. Data collected from wind directions of True bearing 10°-105° will be accepted in this test. This was decided as this direction gave the most open sector to clean free stream. Even though this direction was the best for this test it still is not ideal, it just happens to be the most open direction on the site. To achieve better accuracy of wind measurements the RS was spun ONLY in clockwise direction. This way the downwash of the RS will be directed away from the weather station tower, that is installed in the proximity of the RS. This will ensure less affected wind to the weather station. The station is located at approx true bearing of 120°.When RS is spun clockwise the downwash is directed more westbound. Atmospheric conditions will be recorded on the test day to properly allinging CFD simulations with reality. Extra care was taken to ensure that all factors of atmospheric conditions were taken into account. So as to align the simulation inputs as colesly as possible with the measured conditions.

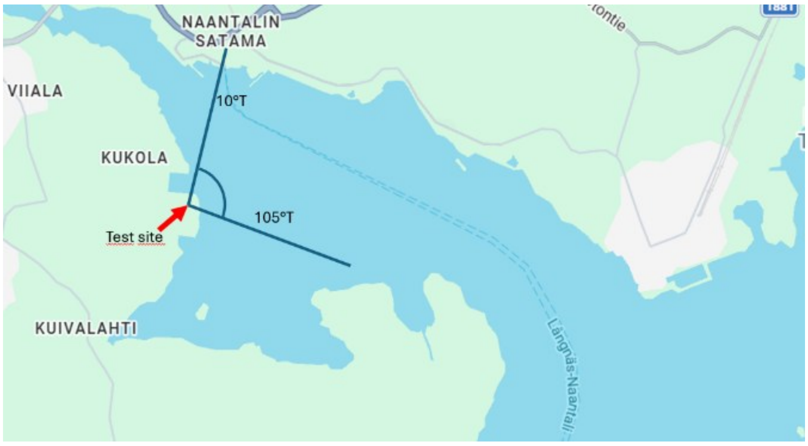

Figure 18: Map of accepted wind direction

Assumptions:

1. By creating constraints to the following parameters such as, spin direction, wind direction, wind speed, the most controlled conditions are achieved, and atmospheric recordings are **considered reliable**.
2. Recorded wind direction was off due to wind sensor systematic misalignment. As wind direction was visually confirmed during testing to stay in set geographic parameters and precise wind angle does not concern this study -> **Wind direction is OK**

The CFD data used in this test has an updated model to better simulate the actual site. This model consists of the updated foundation of RS, including the concrete foot, the foundation adapter as well as the strain gauge segment. The simulation setup can be seen in Figure 19. The simulation also includes wind shear created by the ground boundary layer. This is simulated with a simple equation of

$U(z) = U_{ref} * \left(\frac{z}{Zref}\right)^{A}$, where:

$U_{ref} = AWS_{raw}$ i.e. raw readings from wind sensors

$Z_{ref} = 24.5m$ i.e. height of upper sensor

$A = 0.07$ i.e. Shear exponent derived from NATE Anemometers when AWA 5-50

The exponent governs the effect of ground shear and an exponent of 0.07 was used in this equation. This exponent was picked based on an empirically informed estimate made by professionals in the aerodynamics department of Norsepower. The estimate was based on observations made by two wind sensors located at different height that were roughly at the same position.

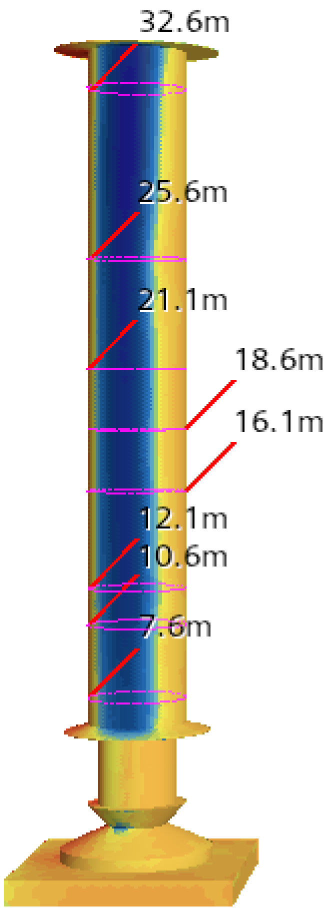

Figure 19: Sensor heights: 1 = 7.6m 5=10.6m, 6=12.1m 7=16.1m, 8= 18.8m, 9=21.1m, 10=25.6m, 12= 32.6 (INOP)

7.3.1 Wind test 8.4.2026.

Test day log:

13:39 RPM 100-> 86. Will drive for ~30min at RS2 state.

13:42 Air pressure = 1029, temp= 8c

13:48 Recorded time at this time is 10:48 UTC in DAQ

14:21 From 86 rpm to 129

14:38 Wind between 5.5m/s and 8.5m/s Closer to SR = 4

15:06 Rpm to 100

15: xx RPM to 130, missing precise time

15:52 Wind direction keeping stable, wind rose closer to 10m/s. Visual inspection of sea with Bofort scale closer to 6.5m/s, wind strength just under of creation of stable white horses.

15:54 Wind speed went under 3.5m/s. Either data is not correct, or wind sensor in very turbulent flow, or the actual wind above ground level is turbulent. At his wind direction (close to 215 true north, wind angle not corrected, and error is known) the wind sensors should be open to pure wind.

16:08 rpm to 80

16:31 rpm to 105

17: xx rpm to 70

17:55 Wind direction keeping steady.

18:15 End of test

The scope of this work is to present viewable data in plotting. The dataset that we are going to work with has almost 5h of data at 1 sec intervals, so the first step in this process is to pick the most stable data to concentrate on. The main objective of this first process is to extract that knowledge. In this work CFD simulated data will be used. A Python script was created to figure out the most stable SR and RPM conditions for CFD simulations. The challenge was that in real use, airflow conditions are highly unsteady. Both wind speed and Spin Ratio vary over time considerably. This makes it difficult to isolate the representative operation points using simple threshold filtering alone. Therefore, a structured computational workflow was developed using multiple python-based scripts to seek the targeted operational conditions.

The raw measurement data originates from the windy day test that was performed on 8.4.2026. On this day the RS was spun during variable wind conditions. Wind direction, air pressure, and temperature were sufficiently constant during these tests. The dataset consists of time-stamped measurements that were sampled at 1 second interval. Each timestamp includes Wind, Rpm and various Force measurements. While the exact data is not included in this thesis due to confidentiality the structure of the data is visible (Table 1). The first stage of analysis focused on understanding the collected data. To see the overall behaviour of Spinratio (SR) and its relationship with windspeed a simple script was created (SpinRatio_plot.py [31]). This script was able to create a rudimentary graph of this relationship (Figure 20). As seen from the leftmost graph the data is unreadable for the human eye. This is why a rolling average was implemented to better understanding of this graph. The middle and right graph show a rolling average of 5min and 15min respectively. This was done to better understand the trends of the data. This early visualisation later formed the foundation for all other filtering decision as they seemed to create natural graphs.

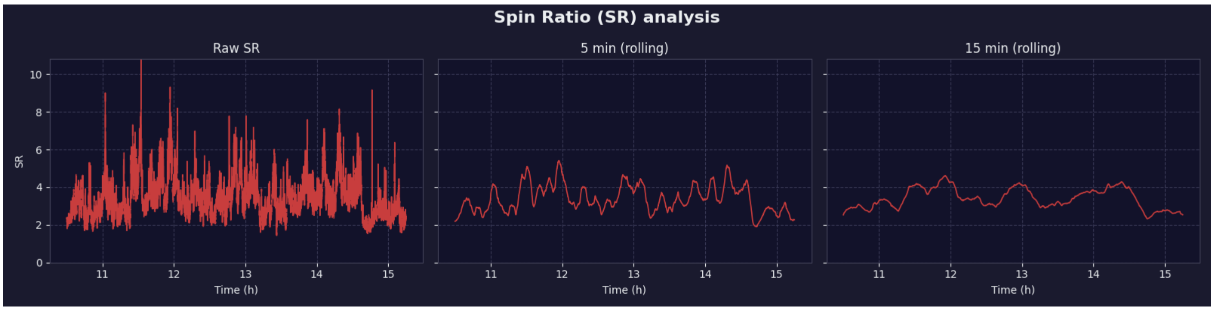

Figure 20: SR analysis of test data

Building on this initial overview, the second stage of analysing this data was to introduce force magnitude and angle analysis through a visualization tool. A script (Force_dir_res_graphtoo.py [31]) was made for this exact reason. This script processes some force data to better visualise the dataset. It graphed all the sensors and visualized their force direction and magnitude values across the full day. This was insightful data as the fluid dynamic effects mentioned in literature review started showing themselves on the plotted graphs. The graphs started to show a trend where the force segment at each sensor exhibited a stronger resultant vector at higher measurement heights. This behaviour is explained by the increase in wind velocity with altitude. This trend can be seen in Figure 21 and moreover when inspecting sensor 10 as it seems to always generate the strongest force vectors. Figure 19 shows the placements of the sensors and some pressure mapping of RS. Figure 22 shows the pressure mapping of the RS more clearly. The figure reveals the uneven distribution of the pressure matrix along the rotor surface. This effect has been documented in literature, however no established naming of this phenomenon has been found during literature review. Hereafter, this phenomenon will be referred to as Boundary-layer Associated Near-tip Aerodynamic Non-linear Asymmetry (BANANA). The naming is based on the fact that this phenomenon is created by the top and bottom hatplates (aka, Thom disc in literature) creating differing boundary layer conditions compared to the Flettner rotor main active area. These effects take place near the active aerodynamic surface area terminus, also known as “Near-tip” in aerodynamic terminology. The phase shift in the pressure field around the rotor is nonlinear and asymmetrical, as the phase shift varies according to the logarithmic windspeed profile, which is inherently non-linear with respect to height. The acronym also reflects the characteristic bilateral curvature of the affected pressure field when both end plates are present. As visible in the Figure 23, the low-pressure field follows the rotor surface upwards and bends in the direction of rotation. This can be observed on both low-pressure and high-pressure sides, although the latter is less distinct due to the automatic scaling of the pressure mapping in the CFD. The CFD simulation setup and result will be discussed later. This phenomenon is caused as a result of the top and bottom hatplates. As when comparing to a flow field of a Flettner Rotos without the bottom plate, the BANANA effect is not visible[8]. The hatplates create a higher efficiency of Magnuss effect in proportion to local effective area. As the hatplates poses surface area that is located at a bigger radius from the spinning axis compared to the rotor surface, the local SR increases. The tips of the pressure zones, illustrated in Figure 23, stretch towards the spin direction as the pressure matrix is inspected closer to the hatplates. As a result, the direction of the force generated by the RS is not always directly proportional to the wind direction, but changes with SR as well. This is one of the reasons why the Test 2: Pressure matrix phase change would bring valuable data. This BANANA phenomena of the pressure matrix can also be seen in Figure 21 on the left side, and the created force magnitude chart of the phenomena is visualized better in Figure 24. It is clear that the resultant vector at the height of sensor 1 has the highest directed angle. Sensor 5 and 6, which are positioned relatively close together (Figure 19), show the transition of the local phase change as examination continues upward. Sensor 7,8 and 9 which again are relatively grouped close together, show nearly exact same force angels. Sensor 10, which is stationed higher to these groups, start to show the transition period of the BANANA phenomena. The phenomena would have been seen best at sensor 12 height, CFD simulations suggest, but at the day of testing this sensor was inoperative.

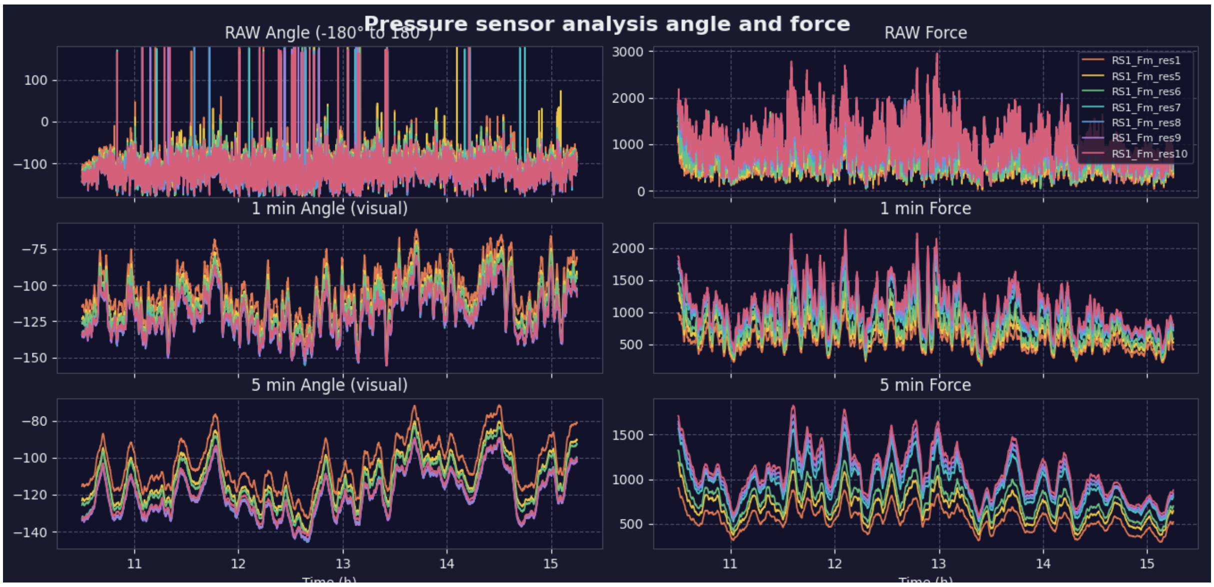

Figure 21: Force calculation plot, MAG and DIR, rolling avg

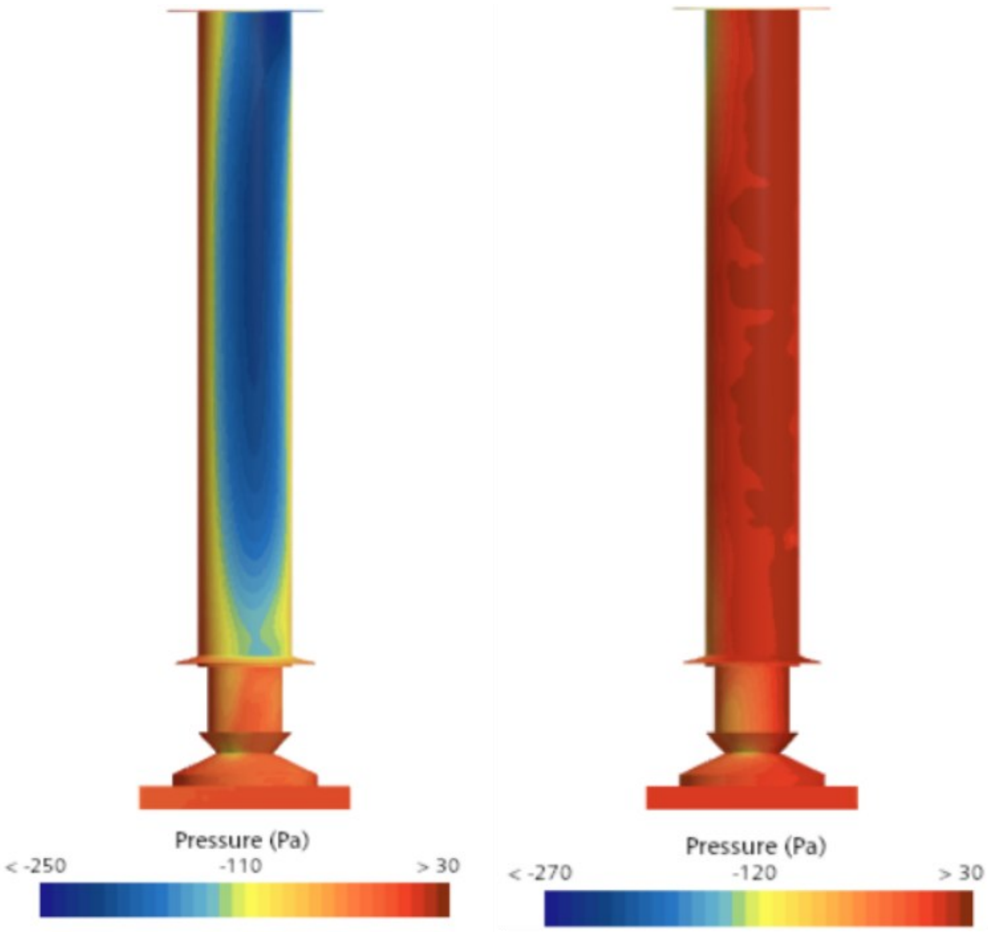

)

Figure 22: Case C simulated pressure zones of both sides of RS.

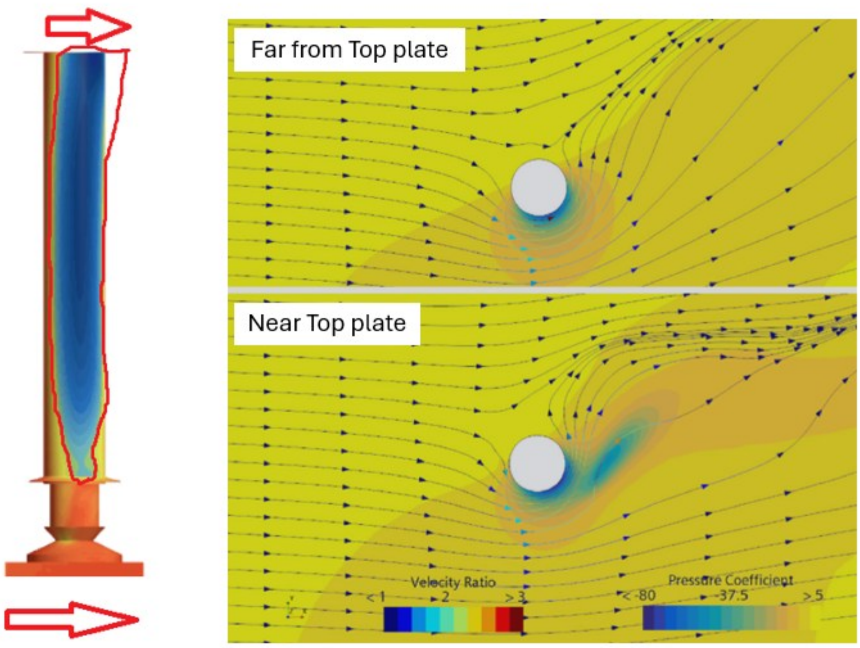

Figure 23: Visualisation of BANANA effect

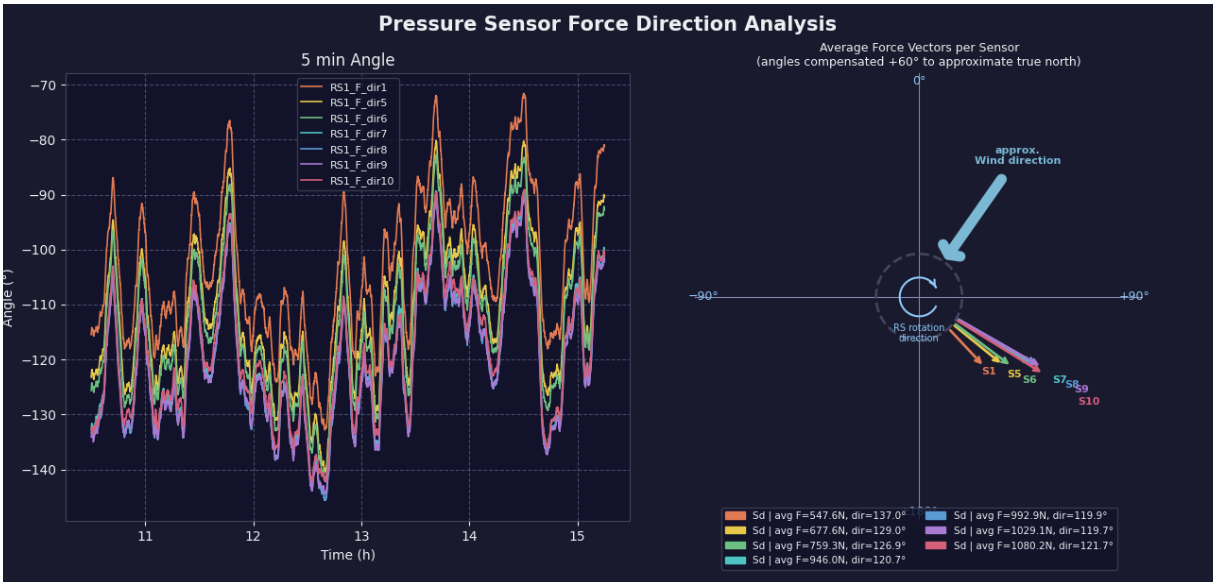

Figure 24: More precise analysis of Figure 19 bottom left plot

Once the system behaviour was understood the next step was to identify the most stable, CFD relevant, wind speed and spin ratio value range. Two filter were applied: Filter A and Filter B. Filter A work principle is to calculate the deviation of a value and see that it stays in tolerance. Filter B further filters the data based on the neighbouring datapoints. Should the values stay consistently in the tolerance area for 5minutes (2.5min before and after) the datapoint is accepted. Visualisation of filters can be seen in

Figure 25. These filters were run on both SR and Apparent Wind Speed (AWS). By implementing a script (CFD_param_extraction.py [31]) that creates clusters of the most reoccurring situations of SR and AWS. After reviewing the data Filter A tolerances of 6% and 8% were chosen, as they provided the most restrictive filtering without reducing the available dataset to an impractical size. A plot (Figure 26) visualises the Forces created at the most reoccurring situations. This plot shows the recorded forces of sensors 1,5 and 10 with a rolling average of neighbouring datapoints applied. After filtering, the dataset is further processed using binning approach. In this method windspeed and Spinratio are discretised into small intervals, and all valid points are grouped according to their nearest bin. This creates a cluster of operating conditions, which can be studied more closely now that they are known. This approach is superior to a simple cut-off filter as this system considers how often does this state return in this condition, favouring conditions that are stable and representative. This distinction is important because CFD validation benefits from repeated occurrences of similar conditions, not just isolated snapshots.

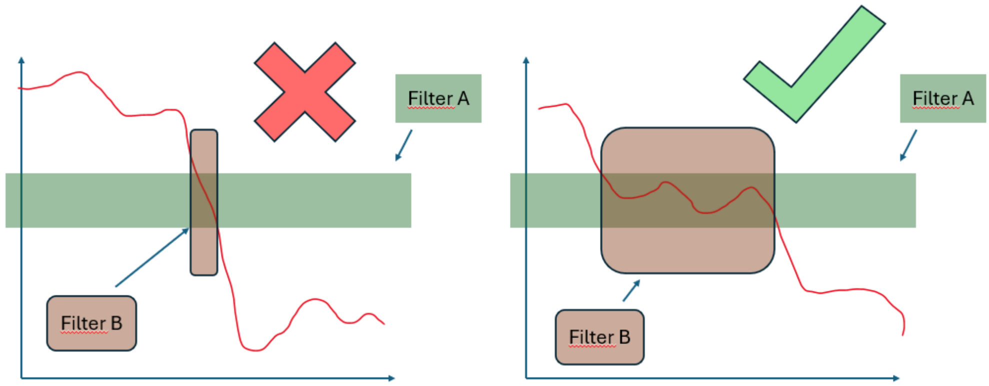

Figure 25: Explanation of filters. Datapoint may only be accepted if 5minutes of neighbouring datapoints fall inside both Filter A and B

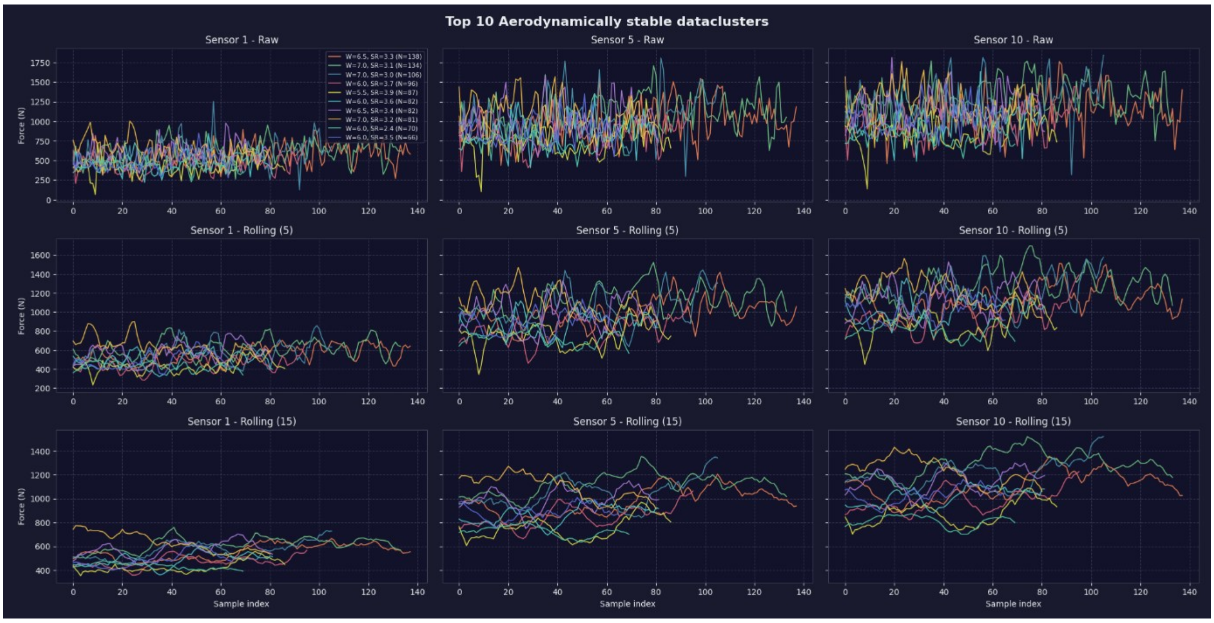

Figure 26: Top 10 Aerodynamically stable dataclusters. X-axis = number of datapoints.

From these clusters the most concurrent situations are extracted. The output of this process can be seen in Figure 26. This figure shows the top 10 clusters with stable wind and SR and where the system spends the most time in these stable conditions. This data is spliced from many different points and thus is quite erratic. For this reason, a rolling average is again implemented to see the data more clearly. The script (CFD_param_extract.py [31]) also outputs the following summary of the plotted data:

Wind ~ 7.00 | SR ~ 3.10 | samples: 134 | Max ±23.0% | Min ±17.3% | Avg ±19.8%
Wind ~ 7.00 | SR ~ 3.00 | samples: 106 | Max ±32.8% | Min ±21.8% | Avg ±26.6%
Wind ~ 6.00 | SR ~ 3.70 | samples: 96 | Max ±25.6% | Min ±21.0% | Avg ±23.0%
Wind ~ 5.50 | SR ~ 3.90 | samples: 87 | Max ±28.8% | Min ±23.6% | Avg ±26.1%
Wind ~ 6.00 | SR ~ 3.60 | samples: 82 | Max ±25.7% | Min ±19.1% | Avg ±22.2%
Wind ~ 6.50 | SR ~ 3.40 | samples: 82 | Max ±27.3% | Min ±20.8% | Avg ±24.1%
Wind ~ 7.00 | SR ~ 3.20 | samples: 81 | Max ±22.6% | Min ±17.8% | Avg ±20.5%
Wind ~ 6.00 | SR ~ 2.40 | samples: 70 | Max ±17.6% | Min ±12.7% | Avg ±14.8%
Wind ~ 6.00 | SR ~ 3.50 | samples: 66 | Max ±24.8% | Min ±17.9% | Avg ±20.5%
TOTAL DATA POINTS: 16920
VALID CFD POINTS: 3866
FILTER REJECTION RATE: 0.7715130023640662

This shows the top 10 clusters with the most datapoints. It displays the Wind and SR condition, their sample count, every clusters biggest and smallest fluctuation between the mean value of each sensor and all of the sensor's average fluctuation. It states the total datapoints in the .csv file of CFD data and the rejected datapoint %. This gives the crucial information on choosing CFD parameters. With Compare_CFD_Windyday.py [31]script these cluster are displayed in Figure 27.

Figure 27: Deeper analysis of filtered data.

The following parameters are chosen for CFD simulation: SR = 3.9, 3.1 and 2.4. These values are chosen as they give both biggest sampling range of SR and have relatively good amount of datapoints. It is important to understand that the amount of data between these cases does differ, as SR 3.1 cluster has 134 samples while the 2.4 has only 70. A reduction of almost 50%. The final extraction phase (Data_extraction.py [31]) focuses on querying specific knowledge of RPM of the rotor for these situations. As from the test day log can be observed the rpm are kept constant for most of the duration of the test. In a perfect world the sail would have kept the RPM precise and constant during the test, but small fluctuations in its spinning speed are predictable (+-1.5RPM), thus this script tells the mean RPM. With the knowledge provided by this script we now know that speeds of 103, 104 and 70 RPM are chosen for these simulations. In conclusion these values were chosen because of data abundance, stability, and physical relevance. The chosen cases correspond to the following representative conditions:

Case A: SR of 3.9, wind 5.5 m/s, 103 RPM, Temperature 8c, Ambient pressure of 1029hPa
Case B: SR of 3.1, wind 7 m/s, 104 RPM, Temperature 8c, Ambient Pressure of 1029hPa
Case C: SR of 2.4, wind 6 m/s, 70 RPM, Temperature 8c, Ambient Pressure of 1029hPa

With the data fully processed, a cross reference method was preformed. When inspecting figures of these tests (Figure 28 and Figure 29) there is a clear trend. As sensor height increases along the RS, the agreement between CFD predictions and measured values improves; however, above approximately the height of sensors 7 and 8, the simulated force magnitudes begin to exceed the measured values. This trend is made more clear with vertical chart in Figure 30, Figure 31 and Figure 32. In these figures a trendline is fitted that resembles a boundary layer distribution. This trendline is fitted using the SciPy library curve_fit function. This function resembles the form of a boundary layer, as it seems to fit the data. It should be noted that given the limited number of datapoints (n = 7) virtually any function based graph can be fitted on this dataset with reasonable visual confirmation sucsess. The used trendline function $\Delta(\mathrm{h}) = C * \left(\frac{h}{h_{ref}}\right)^{A} + D$ where h is sensor height, h_{ref} is 7.6m the lowest sensor, A is the exponent that governs the function steepness, C is for scaling and D constant offset. As the function is run it fits the best numbers to the equation. The resulting trendline seems to be plausable and consistent with visual inspection, and is expected with the ground affected boundarylayer behavior. The graph also contains a green dotted line to indicate the height of the wind sensor on testsite. This is done for clarification to show the measuring height of these tests. From this graph it is possible to conclude that with tighter test sample margins, better recording of atmospheric variables such as restricted wind direction sector, ambient pressure and temperature, it is possible to bring simulation solutions closer to reality. Within the Norsepowers (NATE vs CFD 23-02-2026 JVo) internal reporting it was made clear that CFD gave on average 10 to 12% smaller simulated measurements of force, compared to actual test site measurements. And with this test it can be concluded that simulation margins can be improved.

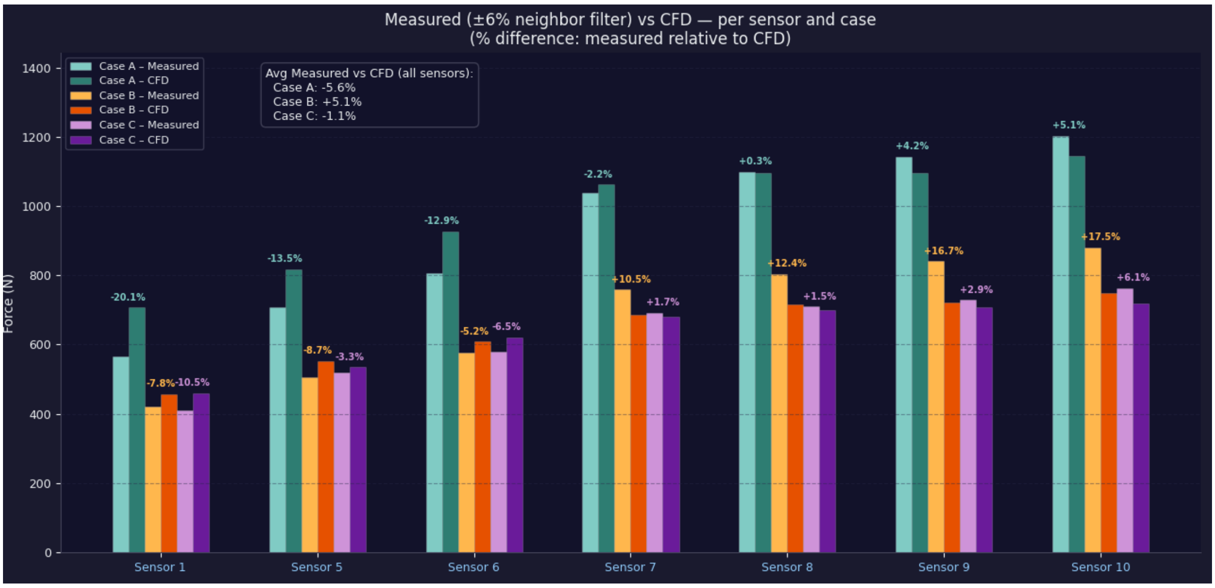

Figure 28: Comparison of CFD and measured +-6%

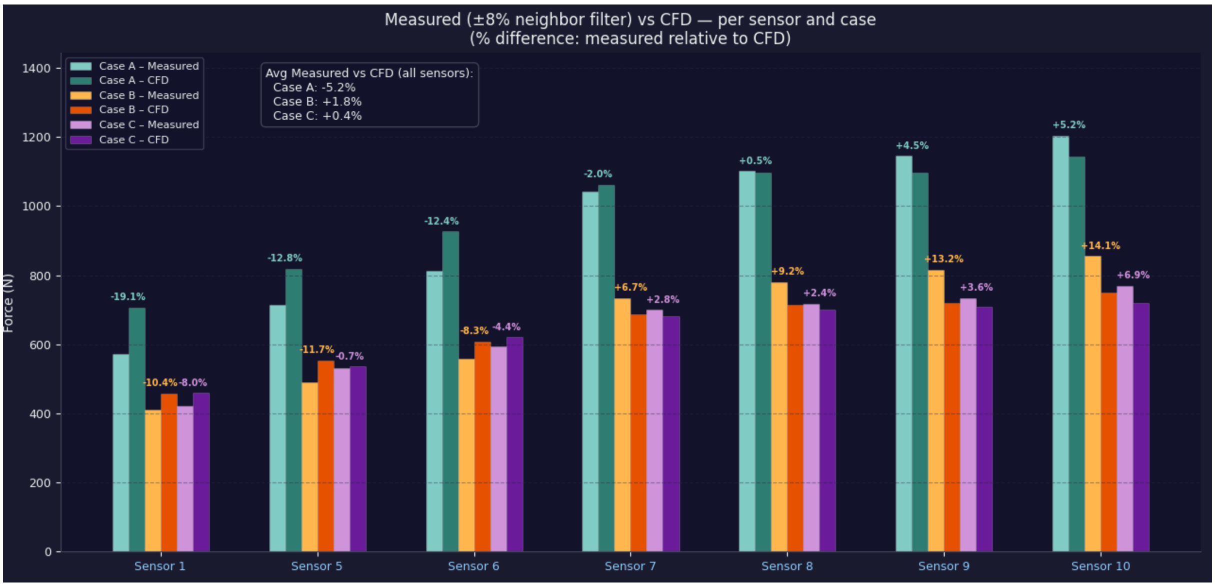

Figure 29: Comparison of CFD and measured +-8%

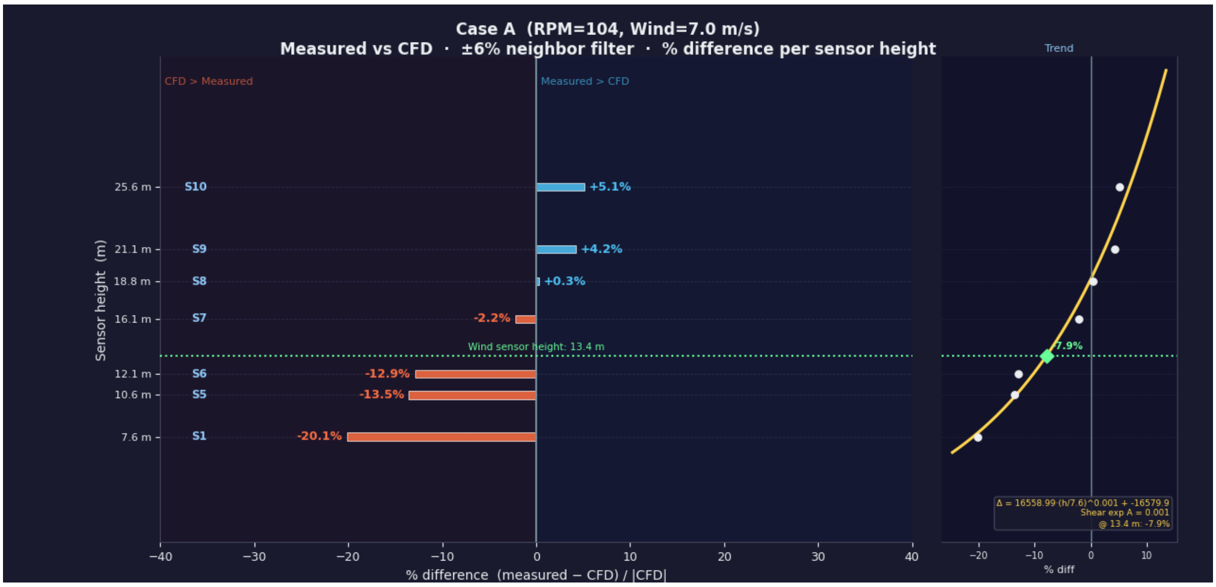

Figure 30: Vertical bar chart case A

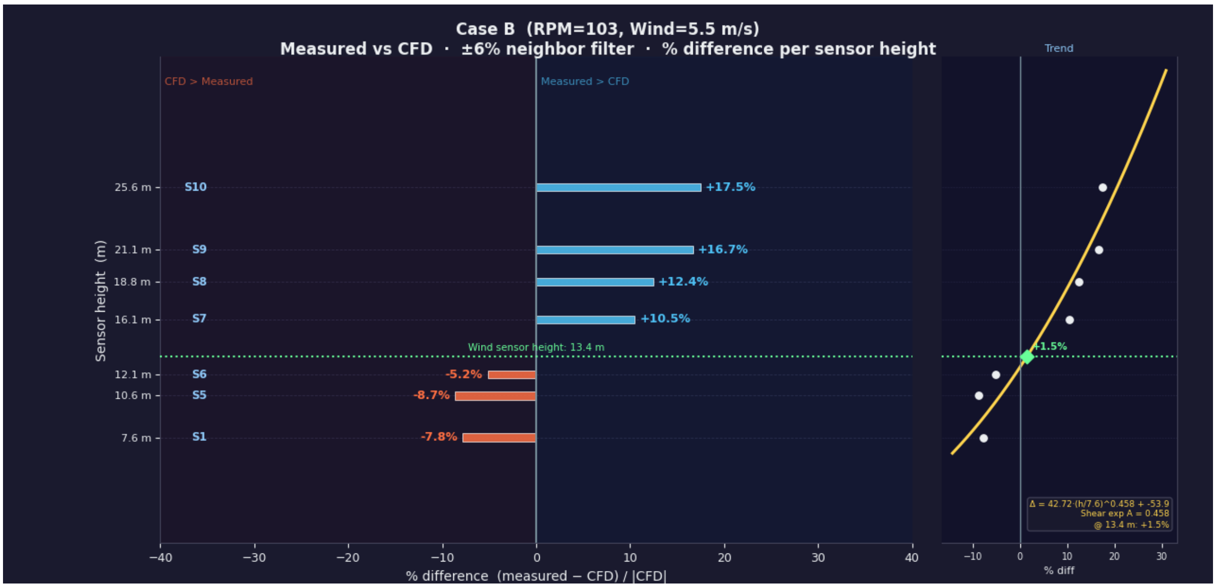

Figure 31:vertical bar chart case B

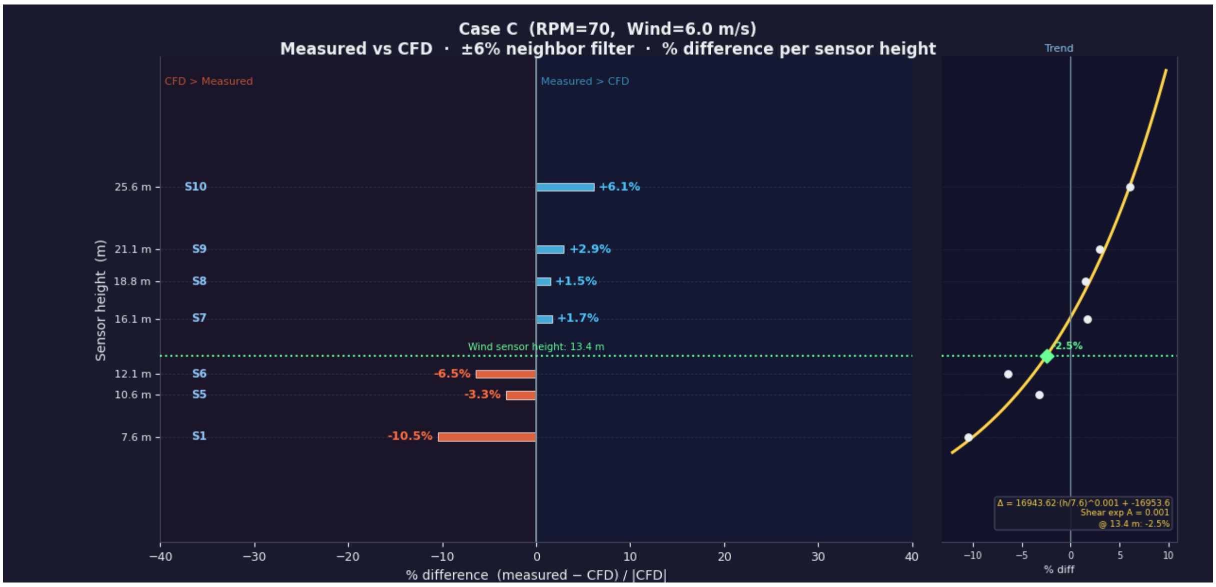

Figure 32: Vertical Bar chart case C.

Colum name	index	Function
_time	0	Pressure sensor dependant force data.
RS1_FM_FWD1	1	Force vector in FWD direction according to every pressure sensor (per 1m height of sail)
RS1_FM_FWD10	2	
RS1_FM_FWD5	3	
RS1_FM_FWD6	4	
RS1_FM_FWD7	5	
RS1_FM_FWD8	6	
RS1_FM_FWD9	7	
RS1_FM_LAT1	8	Force vector in LAT direction according to every pressure sensor (per 1m height of sail)
RS1_FM_LAT10	9	
RS1_FM_LAT5	10	
RS1_FM_LAT6	11	
RS1_FM_LAT7	12	
RS1_FM_LAT8	13	
RS1_FM_LAT9	14	
RS1_F_DIR	15	The resultant force direction
RS1_F_MAG	16	The resultant force magnitude
RS1_F_dir1	17	Force vector direction according to every pressure sensor (per 1m height of sail)
RS1_F_dir10	18	
RS1_F_dir5	19	

RS1_F_dir6	20	
RS1_F_dir7	21	
RS1_F_dir8	22	
RS1_F_dir9	23	
RS1_Fm_res1	24	Force vector direction according to every pressure sensor (per 1m height of sail)
RS1_Fm_res10	25	
RS1_Fm_res5	26	
RS1_Fm_res6	27	
RS1_Fm_res7	28	
RS1_Fm_res8	29	
RS1_Fm_res9	30	
RS1_RPM_ACT	31	
AWA_ACT	32	Apparent Wing Angle Actual (uses the more reliable/stable of the two wind sensors)
AWA_PS_RAW	33	Apparent Wind Angle Sensor 1
AWA_STB_RAW	34	Apparent Wind Angle Sensor 2
AWS_ACT	35	Apparent Wind Speed Actual (uses the more reliable/stable of the two wind sensors)
AWS_PS_RAW	36	Apparent Wind Speed Sensor 1
AWS_STB_RAW	37	Apparent Wind Speed Sensor 2

Table 1: Structure of the test data

8 Results

8.1 Limitations

Several limitations should be noted when interpreting the results of this work.

The test programme included three planned measurement tests. Test 2: Pressure matrix phase change, which could have evaluated the positional accuracy of the pressure sensor readings, was not conducted owing to time constraints and safety considerations during the thesis period. As Test 1 and Test 2 were both designed to answer Q2, this question still stands as only half proven. The outcome of this test would have validated the angular accuracy of the measured resultant force vector. Nonetheless this test would have not provided any confirming findings of the measured force magnitude. Given that the remaining tests demonstrate acceptable agreement in force magnitude, the absence of this test is noted as a limitation but does not undermine the principal conclusions of the study. Test no.2 is recommended as a subject of further study and should be prioritised to give concrete proof in answering Q2.

The CFD simulation used in Test 3, comparing all data across all measuring methods. rely on a wind shear exponent estimated from two anemometers at differing heights. This gave a coarse approximation on the local NaTe wind boundary layer, which after the test was proven to be the most likely cause to create differing simulated results from measured values. The results should be interpreted as representative of tested conditions, and not full scale generalized across all atmospheric variables.

Two further practical limitations affected the scope of this study. Pressure sensor 12 was inoperative at the time of testing, which would have presented the effects of BANANA more clearly. Now the observation of this effect is studied in a combination of CFD simulation, and the measured data at lower heights of the rotor. The conclusion of this effect is for this reason more speculative. Additionally, the strain gauge measurement system installed on RS was not fully operational during the preformed tests. Some inconsistencies, that might be the result of poor calibration, were found. As the window for this thesis did prevent further testing, other from the ones that were preformed, this measuring was dropped from the cross-comparison section of this thesis. One of the limitations for suitable test days were the set parameters on atmospheric conditions. The measuring of strain gauge data would have provided a independent measurement-based validation for CFD and Pressure sensing methods.

8.2 Conclusions

This thesis evaluated the propulsion measurement and estimation methods applicable to Flettner Rotors and validated the reliability of the pressure-sensor based system deployed on Norsepower RotorSails through experimental testing, and CFD comparison. The central questions was whether the installed measurement system produced force estimates that were sufficiently reliable to be trusted for performance reporting and operational purposes.

The literature review and measurement survey presented in Chapters 2-4 establish that four distinct methods exist for quantifying RotorSail propulsion. Surface pressure sensing, strain gauge measurement, CFD simulation and the On-Off method. These differ fundamentally in whether they constitute direct continuous measurements or indirect one-time estimates that can be built up for a predictive algorithm, based on measured atmospheric variables. Each type inhibits trade-offs in accuracy, practicality and the degree of which what concrete function they are measuring.

During pressure data acquisition, a periodic interference signal was identified in the recorded data (Test 1). The frequency of this interference corresponded to 50 Hz, which is consistent with the AC mains supply frequency used in the test environment. While the exact source was not isolated, the frequency does correspond with the EU standard of 230V 50Hz main grid power. A possibility of the interference in pressure sensor signal coming from main powerlines had been found. In absolute terms, the interference amplitude was approximately 1.65Pa. To contextualise the effect of this interference; the RotorSail surface pressure varied approximately 390Pa in CFD simulations used in this thesis. This places the interference of 1.65Pa at approximately 0.4% of the observable signal range. Relative to the full measurement range of the installed absolute pressure sensors, the interference is negligible as it stands on the order of (<0.01%) of the sensor's total measuring range. This signal quality assessment speaks partially to Q2, as it shows that the sensor signal itself is electronically clean enough that no meaningful distortion is introduced at the hardware level. Another result of this thest was the observation that suggests that a pressure sensor with a smaller measuring range should be used to decrease inaccuracies. However, despite this analysis it was determined that the interference does not compromise the integrity of the recorded pressure data. The measurements are sufficiently reliable for force calculation purposes.

Following the assessment of signal quality, the accuracy of the pressure-derived force calculations was evaluated through comparison with CFD simulations (Test3), which together with Test 1 forms the basis for answering Q3. The methodology adopted in this study differs from earlier conducted research in an important respect: rather than simulating and comparing the total resultant force across the entire RotorSail, this study resolved the comparison at the level of individual pressure sensor segments. For each sensor position, a full rotational pressure map was recorded, and the measured pressure was assumed representative of a 1-meter-height strip at that position. The force contribution of each strip was then calculated and compared against the corresponding segment in the CFD model. This segment-by-segment comparison, combined with a tightly controlled set of added test parameters, reduced the deviation between measured and CFD-simulated resultant forces from the approximately 12% reported in earlier company studies to approximately 5%. The CFD comparison also revealed a systematic discrepancy between simulated and measured segment forces. This error pattern is most likely attributed, on the basis of the shown data, to the wind shear exponent used in the simulation. For the preliminary simulations, the exponent was estimated by applying a modest upward correction to the standard flat-terrain value to account for the additional surface roughness introduced by structures at the NaTe test site. This estimate was done with a crude analysis based on two wind sensors positioned at different heights. While this is a reasonable first approximation, it represents only an educated guess because of the small number of datapoints. The wind shear profile at any given test site is directionally dependent. Structures surrounding the test site introduce localised flow disturbances and modify the vertical wind profile differently depending on the approach direction. At the segment level, this produces deviations as large as 20% at certain heights when comparing individual measured and simulated force contributions. This discrepancy would not be visible when comparing only the resultant force vectors. The tests conducted for this thesis were performed in a wind direction selected to minimize the influence of surrounding structures on the free airstream. To achieve further improvement in simulation accuracy a systematic characterisation of the wind shear exponent across the full directional range, CFD boundary conditions could be made direction specific bringing simulated results closer to the measured ones.

The results of the studies performed in this thesis support the conclusion that the Norsepower Rotor Sail™ propulsion measurement system produces reliable force measurements. The pressure data is of acceptable quality, the force calculation methodology is sound, and the deviation between measured and CFD simulated resultant forces is within acceptable bounds given the current simulation setup. The principal sources of the remaining discrepancy have been identified, and steps towards resolving them have been outlined. This thesis provides compelling quantitative evidence that the force measurements produced by the system are in close agreement to physically credible values.

9 Sources

[1] M. Corradi and C. Tacchella, 'A brief history of the Flettner ship, an archetype of sustainable marine propulsion design', TUR, 2023. Accessed: Jan. 19, 2026. [Online]. Available: https://unige.iris.cineca.it/handle/11567/1158172

[2] 'The Magnuss Effect in Theory and Reality'. Accessed: Feb. 23, 2026. [Online]. Available: https://digital.library.unt.edu/ark:/67531/metadc63663/m2/1/high_res_d/19930094847.pdf

[3] 'World Energy Outlook 2025 – Analysis', IEA. Accessed: May 12, 2026. [Online]. Available: https://www.iea.org/reports/world-energy-outlook-2025

[4] 'About IMO GreenVoyage2050: GreenVoyage2050'. Accessed: Oct. 15, 2025. [Online]. Available: https://greenvoyage2050.imo.org/about-the-project/

[5] N. Rehmatulla, J. Calleya, and T. Smith, 'The implementation of technical energy efficiency and CO 2 emission reduction measures in shipping', *Ocean Engineering*, vol. 139, pp. 184–197, Jul. 2017, doi: 10.1016/j.oceaneng.2017.04.029.

[6] J. Seifert, 'A review of the Magnus effect in aeronautics', *Progress in Aerospace Sciences*, vol. 55, pp. 17–45, Nov. 2012, doi: 10.1016/j.paerosci.2012.07.001.

[7] J. Seifert, 'A review of the Magnus effect in aeronautics', *Progress in Aerospace Sciences*, vol. 55, pp. 17–45, Nov. 2012, doi: 10.1016/j.paerosci.2012.07.001.

[8] C. S. Kwon, S. M. Yeon, Y. C. Kim, Y. G. Kim, Y. H. Kim, and H. J. Kang, 'A parametric study for a flettner rotor in standalone condition using CFD', *International Journal of Naval Architecture and Ocean Engineering*, vol. 14, p. 100493, Jan. 2022, doi: 10.1016/j.ijnaoe.2022.100493.

[9] P. et Ackeret, *Français : Animation de la Polaire du navire Buckau à 2 rotors de Flettner, d'après le Technical Memorendum NACA TM N° 367, Application of the Magnus effect to the wind propulsion of ships, L. Prandtl [1]. La lecture de cette courbe 'polaire' se fait comme suit : Pour chaque cap du bateau par rapport à son vent apparent[1], suivre son axe (devant lui) : l'interception de cet axe avec les deux courbes donne l'intensité de la force de propulsion produite par le vent (à mesurer depuis l'origine des axes à cette intersection). La zone hachurée de la courbe bleue (qui se place aux 'allures portantes') représente la diversité des forces véliques qui peuvent exister selon l'adaptation des voiles à la force du vent (selon que l'équipage se donne le mal d'établir toute la voilure possible ou qu'il conserve une voilure réduite)...* 1925. Accessed: May 27, 2026. [Online]. Available: https://commons.wikimedia.org/wiki/File:Anim_Polaire_Buckau.gif

[10] Previously Posted Online, *1925 to 1929 Popular Science*. 1927. Accessed: May 27, 2026. [Online]. Available: http://archive.org/details/1925-to-1929-popular-science

[11] 'Full-Issue-Vol-36-Issue-2-2016.pdf'. Accessed: Jan. 01, 2026. [Online]. Available: https://www.usp.ac.fj/wp-content/uploads/sites/162/2023/07/Full-Issue-Vol-36-Issue-2-2016.pdf#page=162

[12] 'Always on schedule with rotor sails – a captain tells his story'. Accessed: May 28, 2026. [Online]. Available: https://www.dnv.com/expert-story/maritime-impact/Always-on-schedule-with-rotor-sails-a-captain-tells-his-story/

[13] 'New EU rules aiming to decarbonise the maritime sector take effect - Mobility and Transport'. Accessed: May 28, 2026. [Online]. Available: https://transport.ec.europa.eu/news-events/news/new-eu-rules-aiming-decarbonise-maritime-sector-take-effect-2025-01-10_en

[14] J. Peltomaa, 'SEA-CARGO's tilting Rotor Sails deliver instant operational results', Norsepower Rotor Sails™ | Wind Propulsion. Accessed: Jan. 23, 2026. [Online]. Available: https://www.norsepower.com/post/sea-cargos-tilting-rotor-sails-deliver-instant-operational-results/

[15] 'EEXI and CII - ship carbon intensity and rating system'. Accessed: May 12, 2026. [Online]. Available: https://www.imo.org/en/mediacentre/hottopics/pages/eexi-cii-faq.aspx

[16] A. De Marco, S. Mancini, C. Pensa, G. Calise, and F. De Luca, ‘Flettner Rotor Concept for Marine Applications: A Systematic Study’, *International Journal of Rotating Machinery*, vol. 2016, no. 1, p. 3458750, 2016, doi: 10.1155/2016/3458750.
[17] G. Bordogna *et al.*, ‘Experiments on a Flettner rotor at critical and supercritical Reynolds numbers’, *Journal of Wind Engineering and Industrial Aerodynamics*, vol. 188, pp. 19–29, May 2019, doi: 10.1016/j.jweia.2019.02.006.
[18] W. Chen, H. Wang, and X. Liu, ‘Experimental investigation of the aerodynamic performance of Flettner rotors for marine applications’, *Ocean Engineering*, vol. 281, p. 115006, Aug. 2023, doi: 10.1016/j.oceaneng.2023.115006.
[19] D. Massaro, M. Karp, N. Jansson, S. Markidis, and P. Schlatter, ‘Direct numerical simulation of the turbulent flow around a Flettner rotor’, *Sci Rep*, vol. 14, no. 1, p. 3004, Feb. 2024, doi: 10.1038/s41598-024-53194-x.
[20] X. Hu, F. Malizia, and B. Blocken, ‘CFD simulations of running aerodynamics: Impact of computational parameters’, *Journal of Wind Engineering and Industrial Aerodynamics*, vol. 268, p. 106271, Jan. 2026, doi: 10.1016/j.jweia.2025.106271.
[21] Y. Zhao, Y. Liu, Y. Li, and Q. Hao, ‘Development and Application of Resistance Strain Force Sensors’, *Sensors (Basel)*, vol. 20, no. 20, p. 5826, Oct. 2020, doi: 10.3390/s20205826.
[22] A. A. Barlian, W.-T. Park, J. R. Mallon, A. J. Rastegar, and B. L. Pruitt, ‘Review: Semiconductor Piezoresistance for Microsystems’, *Proceedings of the IEEE*, vol. 97, no. 3, pp. 513–552, Mar. 2009, doi: 10.1109/JPROC.2009.2013612.
[23] D. R. França and A. Blouin, ‘All-optical measurement of in-plane and out-of-plane Young’s modulus and Poisson’s ratio in silicon wafers by means of vibration modes’, *Meas. Sci. Technol.*, vol. 15, no. 5, p. 859, Mar. 2004, doi: 10.1088/0957-0233/15/5/011.
[24] V. Vigna and M. Figari, ‘Wind-Assisted Ship Propulsion: Matching Flettner Rotors with Diesel Engines and Controllable Pitch Propellers’, *Journal of Marine Science and Engineering*, vol. 11, no. 5, p. 1072, May 2023, doi: 10.3390/jmse11051072.
[25] P. Räisänen, *Laivatekniikka: modernin laivanrakennuksen käsikirja*, 2. korj. p. Turku: Turun ammattikorkeakoulu, 2000.
[26] ‘United States Naval Academy. (n.d.). Resistance and powering of ships (Chapter 7). EN400 Principles of Ship Performance course notes. Chapter 7’.
[27] ‘cooley-tukey.pdf’. Accessed: May 07, 2026. [Online]. Available: https://web.stanford.edu/class/cme324/classics/cooley-tukey.pdf
[28] ‘scipy.signal.hann — SciPy v0.13.0 Reference Guide’. Accessed: May 25, 2026. [Online]. Available: https://docs.scipy.org/doc/scipy-0.13.0/reference/generated/scipy.signal.hann.html?utm_source=chatgpt.com
[29] ‘hann - Hann (Hanning) window - MATLAB’. Accessed: May 25, 2026. [Online]. Available: https://www.mathworks.com/help/signal/ref/hann.html
[30] ‘Microsoft Word - datasheet04022INDPRO_04’. Accessed: May 04, 2026. [Online]. Available: https://docs.rs-online.com/ffcd/0900766b812c4100.pdf
[31] ‘Aleksander Gävert / Flettner rotor Propulsion measurement and authentication · GitLab’, GitLab. Accessed: Jun. 16, 2026. [Online]. Available: https://gitlab.utu.fi/magave/flettner-rotor-propulsion-measurement-and-authentication
[32] P. Duhamel and M. Vetterli, ‘Fast fourier transforms: A tutorial review and a state of the art’, *Signal Processing*, vol. 19, no. 4, pp. 259–299, Apr. 1990, doi: 10.1016/0165-1684(90)90158-U.
[33] ‘Discrete Fourier Transform — NumPy v2.4 Manual’. Accessed: May 20, 2026. [Online]. Available: https://numpy.org/doc/stable/reference/routines.fft.html